Pacific Northwest
NATIONAL LABORATORY

PNNL-30068

Validation of Computational Fluid Dynamics Simulations for the Biological Performance Assessment of Hydropower Generation Units

Final Report

April 2021

Rajesh K Singh
Marshall C Richmond
Pedro Romero-Gomez
Cynthia L Rakowski
John A Serkowski

DISCLAIMER

This report was prepared as an account of work sponsored by an agency of the United States Government. Neither the United States Government nor any agency thereof, nor Battelle Memorial Institute, nor any of their employees, makes **any warranty, express or implied, or assumes any legal liability or responsibility for the accuracy, completeness, or usefulness of any information, apparatus, product, or process disclosed, or represents that its use would not infringe privately owned rights**. Reference herein to any specific commercial product, process, or service by trade name, trademark, manufacturer, or otherwise does not necessarily constitute or imply its endorsement, recommendation, or favoring by the United States Government or any agency thereof, or Battelle Memorial Institute. The views and opinions of authors expressed herein do not necessarily state or reflect those of the United States Government or any agency thereof.

Validation of Computational Fluid Dynamics Simulations for the Biological Performance Assessment of Hydropower Generation Units

Final Report

April 2021

Rajesh K Singh
Marshall C Richmond
Pedro Romero-Gomez
Cynthia L Rakowski
John A Serkowski

Summary

The work presented in this report was performed under the HydroPASSAGE project (www.hydropassage.org) and includes validation and model confirmation for the computational fluid dynamics (CFD)-Biological Performance Assessment (BioPA) modeling tools. The BioPA toolset developed by Pacific Northwest National Laboratory (PNNL) is used in combination with CFD simulations to predict the relative risk of injury and mortality that fish may experience during hydropower turbine passage. Biological response models, often called dose-response models, were developed in laboratory tests using fish exposed to stressors like those associated with passage through hydropower facilities. The BioPA toolset combines the biological response models with particle trajectories and impacts through CFD analysis to predict a relative risk. The resulting relative risk index scores may be used to refine an original design, compare competing turbine designs, or improve the performance of an existing hydropower turbine.

BioPA toolset Version 3, released in December 2019, utilizes directly computed trajectories and collisions of material particles using CFD simulation codes. Previous versions of BioPA relied on Tecplot CFD post-processing software to compute stream trace trajectories. Presented in this document are a series of tests necessary to validate the updates to the BioPA toolset Version 3. First, the method of particle collision detection was evaluated. The CFD-predicted impact velocity, collision time, velocity field, and trajectory of a sphere closely matched the analytical value for a bouncing ball in the elastic collision. A similar approach was tested and validated for a collision of spheres using a 45° inclined plane. Next, the CFD-predicted trajectories and collisions of the small spherical and cylindrical particles were compared to physical experimental data observed for a vane array and large cylinder in a water flume. Lastly, the CFD-predicted flow field and hydraulic performance of a laboratory-scale Francis turbine and Kaplan turbine models were validated. The trajectory of the particles is significantly affected by the flow field within hydraulic turbines. All CFD-predictions matched closely with experimental models. The BioPA toolset was modified to accept direct outputs of the CFD prediction. This enhancement allows the BioPA toolset Version 3 to model and predict stressors, resulting in a powerful predictive tool for the evaluation of the biological performance of hydroelectric turbines.

Acknowledgments

Acronyms and Abbreviations

BEP	best efficiency point
BioPA	Biological Performance Assessment
CAD	computer-aided design
CFD	computational fluid dynamics
CMS	cubic meter per second
DEM	discrete element method
ERDC	Engineer Research and Development Center, USACE
ESBS	extended-length submersible bar screen
HL	high load
LDV	laser Doppler velocimetry
MCN	McNary Dam, Columbia River
MRF	multiple reference frame
NTNU	Norwegian University of Science and Technology
PIC	PNNL institutional computing
PL	part load
PLM	Product Lifecycle Management
PNNL	Pacific Northwest National Laboratory
PQI	Passage Quality Index
SST	shear stress transport
USACE	U.S. Army Corps of Engineers

Contents

Figures

Tables

1. Introduction

The work presented in this report was performed under the HydroPASSAGE project (www.hydropassage.ord) and includes validation and model confirmation for the computational fluid dynamics (CFD)-based Biological Performance Assessment (BioPA) modeling tools. The BioPA toolset provides a scientifically tested and validated tool to advance fish-friendly passage designs in the hydropower industry. This report documents validation tests of the CFD modeling approach applied to the recent modification of the BioPA toolset. The validation includes the comparison of CFD-predicted hydraulic and flow quantities such as velocity, pressure, particle strikes, particle dispersion, hydraulic efficiency, torque, and net head with the corresponding experimental values. Turbine manufacturers and hydropower operators will be able to advance fish-friendly passage designs through modeling and prediction of fish stressors, thereby expediting regulatory processes, resulting in the rapid development of a more efficient and sustainable hydropower fleet.

1.1 Background

Hydropower facilities represent physical barriers for fish species in both upstream and downstream migrations. While hydropower infrastructure typically incorporates alternative routes for fish to bypass the extreme hydraulic conditions found in passage through turbines, fish bypass efficiencies never achieve 100% (Coutant and Whitnet, 2000). The concept of the fish-friendly hydropower turbines encompasses several improved geometric features in reaction turbines, such as Kaplan and Francis turbines. These improvements include tight tolerances between blades and hubs, reductions in rapid flow redirections, and improved operating conditions throughout the operating range, enhancing the fish survival rate (Hogan et al. 2014). The BioPA toolset, developed by PNNL, predicts the relative biological performance of fish passage through a hydropower unit (Richmond et al. 2014b). The sustainability of hydropower is improved by applying the BioPA toolset and other information developed as part of the U.S. Department of Energy (DOE) Water Power Technologies Office HydroPASSAGE project. Development and application of the BioPA toolset and associated CFD for turbines has benefited from funding and collaboration with end users including the U.S. Army Corps of Engineers (USACE).

The BioPA toolset consists of the four components listed here and described in greater detail below:

1. MODEL - The CFD model that describes the hydraulic environment

2. TRAJECTORIES - The particle trajectories using the flow-particle interaction method

3. PROBABILITIES - Calculation of exposure probabilities to pressures and velocities

4. PASSAGE QUALITY INDEX - Conversion of exposures to a Passage Quality Index (PQI) using biological response data.

1.1.1 Model and Trajectories

The BioPA toolset uses CFD to simulate the hydraulic environment of a potential passage route to estimate the probability of exposure to stressors believed to adversely affect the survival of fish. The previous version of the BioPA toolset, Version 2, relied on calculating stream traces in the flow field, using Tecplot—a commercial CFD post-processing software. In Version 3, stream traces have been replaced with particle trajectories calculated within the CFD code using the

flow-particle interaction method. The CFD simulations, using Lagrangian particle tracking methods, enable the computation of an estimated fish trajectory along with associated stressors (e.g., pressure, velocity, strain rate, etc.). This method also directly detects the collision (or strike) dynamics of the fish with various components of the hydropower unit during entrainment. A typical snapshot for the CFD-computed trajectory with the velocity of particles is shown in
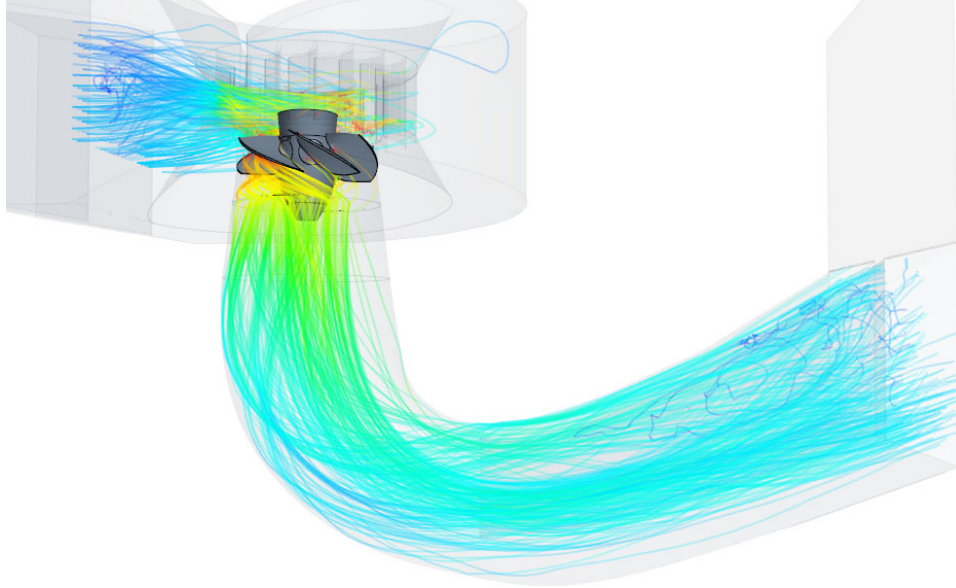
Figure 1. BioPA Version 3 (and future versions) eliminates the post processing software resulting in more efficient results (in terms of software and labor costs) for end users.
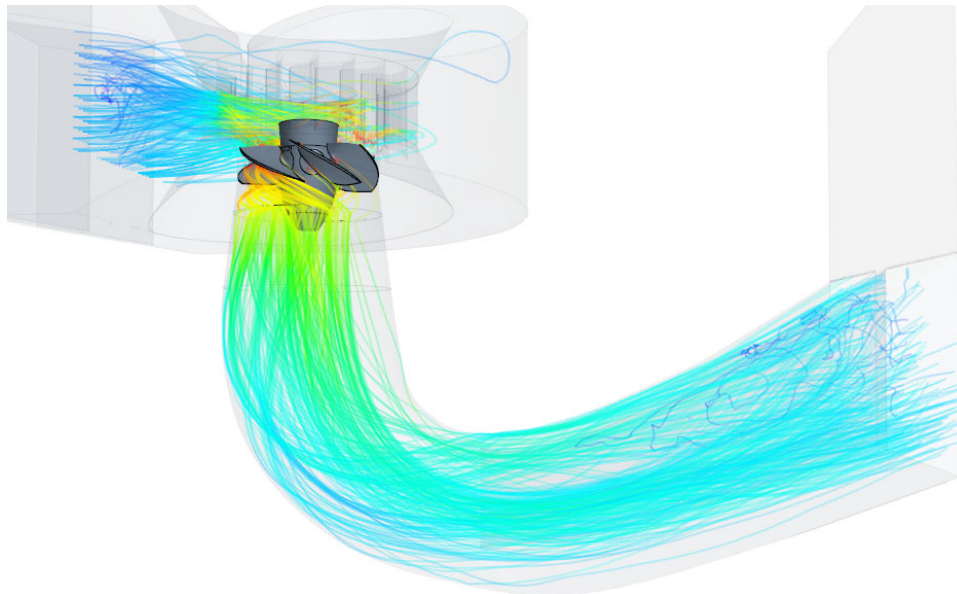
Figure 1. Flow trajectory and velocity in a Kaplan turbine.

1.1.2   Probabilities

Validation and model confirmation of the CFD-BioPA method requires examining studies of associated data sets that can be used to compare model performance to the major biological

stressors of fish in combination with the hydraulic performance metrics of turbines. This validation compares CFD-predicted quantities to the observed data from laboratory experiments and/or field tests.

Hydraulic performance metrics include the following:

– Net head: The effective head difference between the turbine inlet and exit of draft tube

– Efficiency: Overall efficiency of the turbine

– Torque: Measurement of torque on the runner shaft.

Biological stressors include the following:

– Pressure: Pressure field within the hydropower unit

– Collison and blade strike: Particle-based (discrete element method [DEM] spheres/cylinders) simulation of collision intensity and locations

– Hydraulic shear: Shear rate estimates at the scale of a fish

– Turbulence: Random velocities and eddies that can disorient fish and cause decreased hydraulic efficiency.

The stressors listed above are used as inputs for the biological performance evaluation in the fish passage using the BioPA toolset (Richmond et al. 2014a; User Guide: BioPA Toolset 2020).

1.1.3 Passage Quality Index

Passage Quality Index (PQI) is a performance score that can be used to make relative comparisons between run conditions, such as between different turbine designs or operations. The score ranges from 0 to 500, with larger numbers estimated to have higher survival rates (i.e., lower likelihood of adverse passage).

1.2 Objectives

This document provides a summary of the work necessary to establish the computational methods used when generating hydraulic components for the BioPA toolset. The laboratory data sets for testing and validation of the hydraulic components of the BioPA software are identified. In addition to the flow and the hydraulic characteristics, the automated method for extracting the collision data using JavaScript was also validated. The validation of the method was performed by comparing the CFD-predicted collision data set (such as impact velocity, collision time, etc.) with the analytical theory for the elastic collision of a sphere with a flat horizontal wall. The mechanism of collision detection was further validated with the elastic collision of a sphere with an inclined plate. After successful validation testing, numerical methods for CFD simulations can be further employed to predict the hydraulic components for the BioPA toolset using Lagrangian and DEM material particles.

In summary, the tasks performed to achieve validation of the CFD modeling include the following:

- Automated method to extract elastic collision data, sphere on a flat plate
- Automated method to extract elastic collision data, sphere on an inclined plane
- DEM and Lagrangian particle collision with vane array installed in the water flume

- DEM and Lagrangian particle collision with target circular cylinder in the flume experiments
- Flow and hydraulic characteristics of a laboratory model of the Francis turbine (Francis-99)
- Flow and hydraulic characteristics in prototype (full-scale) Kaplan turbine.

1.3 Report Contents and Organization

The ensuing sections of this report describe the methods necessary to validate the enhancements to the tool. First, in Section 2, the collision detection validation methods are described in detail. This consists of CFD simulations for a bouncing ball test, where a ball bounces on a flat plate in air. Next, CFD simulations model a ball bouncing on an inclined plate, where the ball is given an initial velocity and gravity is not considered. In Section 3, flowing water is introduced to the collision detection methods and CFD simulations are used to model particles striking a vane array and a large vertical cylinder. The results of the CFD simulation are compared to physical model experiments. Last, the complex flow fields within hydraulic turbines are compared to CFD model simulations for Francis and Kaplan type turbines. Appendix A provides a brief description of the computation of shear when assessing biological performance.

2.   Collision Detection Validation

2.1 Collision Detection; Sphere on Flat Plate

This section describes the collision detection method employed in the CFD simulations. The collision detection method extracts the strike data set simulating fish passage through the hydropower unit. Accordingly, the CFD simulations were also conducted to validate the collision detection method employed in the extraction of required data for the BioPA toolset. For this purpose, bouncing sphere physics, the elastic collision of sphere with flat horizontal surface, was selected in the CFD simulations. The CFD-predicted impact velocity, collision points, and collision time were compared with corresponding analytical values.

2.1.1   Theoretical Derivation

Bouncing sphere is a problem combining several principles related to acceleration, momentum, and energy. The sphere falls vertically, downward, under the influence of gravity (g = 9.81 m/sce^2) with an initial velocity U_0 in the absence of air resistance.

The collisions of the sphere with the horizontal flat surface are assumed to be instantaneous. The relationship between the velocity of the sphere before, u_n^- , and after, u_n^+ can be expressed as:

$$u_n^+ = -e.u_n^-$$

(1)

Here, e is the coefficient of restitution ($0 \leq e \leq 1$) that accounts the energy loss associated with the collision event. The coefficient of restitution is independent from the impact velocity and only depends on the colliding objects. For completely elastic collisions, its value is unity; subsequently Equation (1) leads to:

$$u_n^+ = -u_n^{-1}.$$

(1)

As mentioned earlier, the sphere is only subjected to gravity. Therefore, the height of the center of sphere at the time interval t_n to t_{n+1} can be expressed as:

$$h(t) = h_n + u_n(t - t_n) - \frac{g}{2}(t - t_n)^2$$

(2)

Here, $h_n = h(t_n)$. The velocity of the sphere is computed as:

$$u_{n+1} = u_n - g(t_{n+1} - t_n)$$

(3)

2.1.2   Computational Simulations

Flow simulations were conducted to compute the trajectory and collision of a sphere with the flat surface. The height of the domain was kept sufficiently large to avoid the collision of the sphere with the top of domain after rebound (see Figure 2). In the simulation, no external forces were considered except the effect of gravity. The flow domain was filled with stagnant air as a primary

phase in which the solid sphere falls and subsequently strikes the bottom. The sphere was released from a height h_0 at initial velocity U_0.
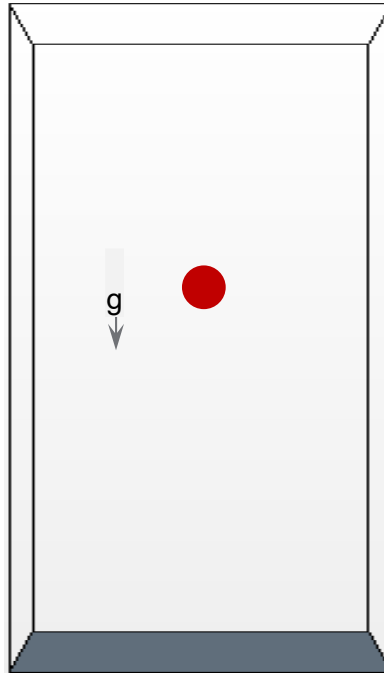
Figure 2.   Schematic of flow domain showing initial position of sphere.

2.1.3   Results and Discussion

Separate flow simulations were conducted for both Lagrangian and DEM spheres. The sphere was released from 0.45 m above the flat surface with an initial velocity of 1.0 m/sec. Collisions of the sphere with the flat surface were detected by boundary sampling methods. A JavaScript function was developed and plugged into the simulation to export the boundary sampling data for each collision event. The CFD-predicted collision times were compared with the analytical values. The collision events for both particle types are also shown in Figure 4 and Figure 6 as Cn (n = 1, 2, ..10). As evident in Table 1, CFD-predicted times for both particles match well with analytical values for each collision event.

Table 1. Comparison of CFD-predicted collision time with corresponding analytical values.

Collison Event	Analytical Value (sec)	CFD Prediction (sec)	
		DEM Sphere	Lagrangian Sphere
First (C1)	0.2176	0.2146	0.2180
Second (C2)	0.8568	0.8471	0.8591
Third (C3)	1.4959	1.4801	1.5021
Fourth (C4)	2.1351	2.1132	2.1470
Fifth (C5)	2.7743	2.7460	2.7939
Sixth (C6)	3.4134	3.3784	3.4427
Seventh (C7)	4.0526	4.0108	4.0936
Eight (C8)	4.6918	4.6428	4.7463

Collison Event	Analytical Value (sec)	CFD Prediction (sec)	
		DEM Sphere	Lagrangian Sphere
Ninth(C9)	5.3310	5.2744	5.4010
Tenth (C10)	5.9701	5.9056	6.0577

As shown in Figure 3 and Figure 5, the CFD-predicted instantaneous height of the sphere compared well with the analytical value computed by Equation (3). A slight discrepancy in the instantaneous height near the bottom is seen for the DEM sphere at the bottom in Figure 5. This is due to DEM physics that account for the surface contact instead of the center of particles during inter-particle or particle/wall interaction leading to an expected increased value of the center-wall distance during collision. Overall, CFD-predicted results excellently match the analytical values.
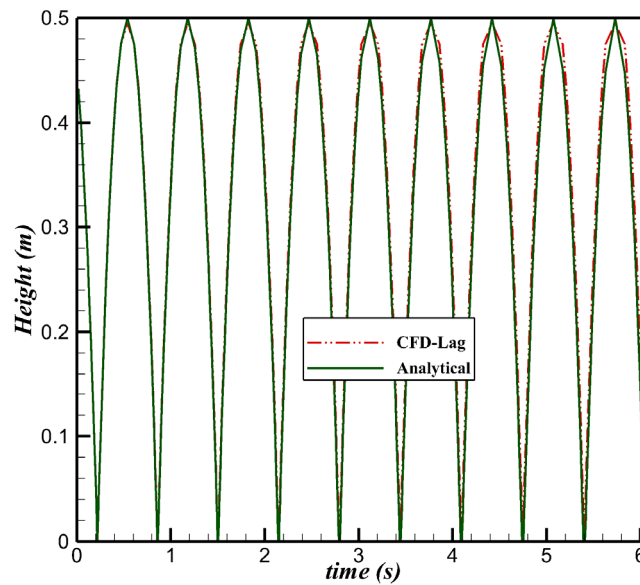
Figure 3.   CFD-predicted height compared to analytic results, Equation (3), Lagrangian Sphere.
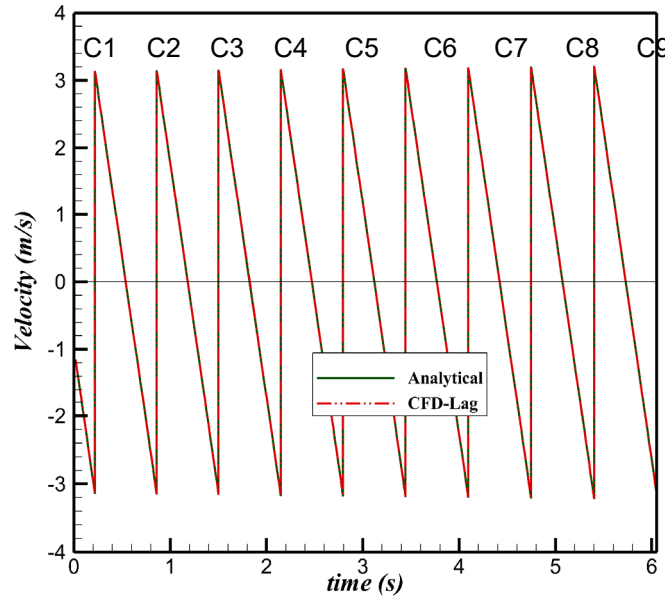
Figure 4.   CFD-predicted velocity compared to analytic results, Equation (4), Lagrangian Sphere. *(Points C1through C9 represent collisions.)*

Next, the CFD-predicted temporal velocity of sphere was compared with the analytical value computed by Equation (4). Figure 5 and Figure 6 show that CFD-predicted velocity computed by both methods excellently matched the analytical value. The sharp jump (vertical line) in the velocity plot depicts the collision event of the sphere. Note that the sign of the velocity only changes after the collision for the elastic collision.
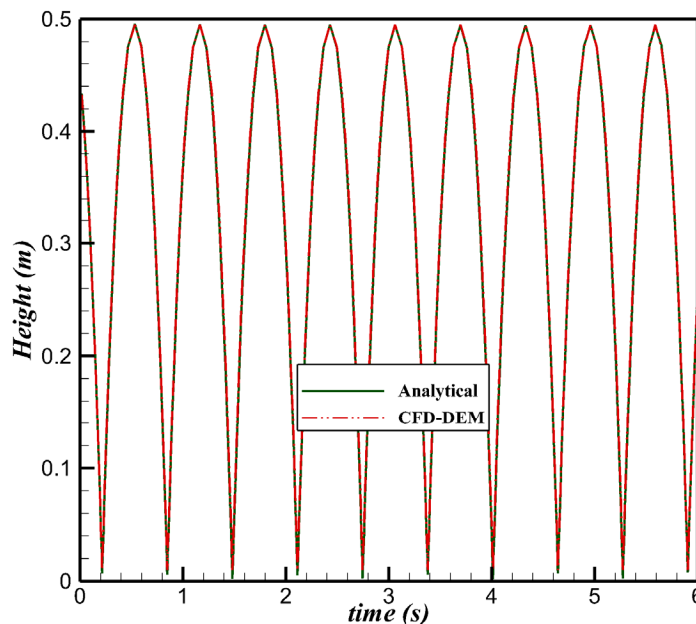
Figure 5.   CFD-predicted height compared to analytic results, Equation (3), DEM sphere.
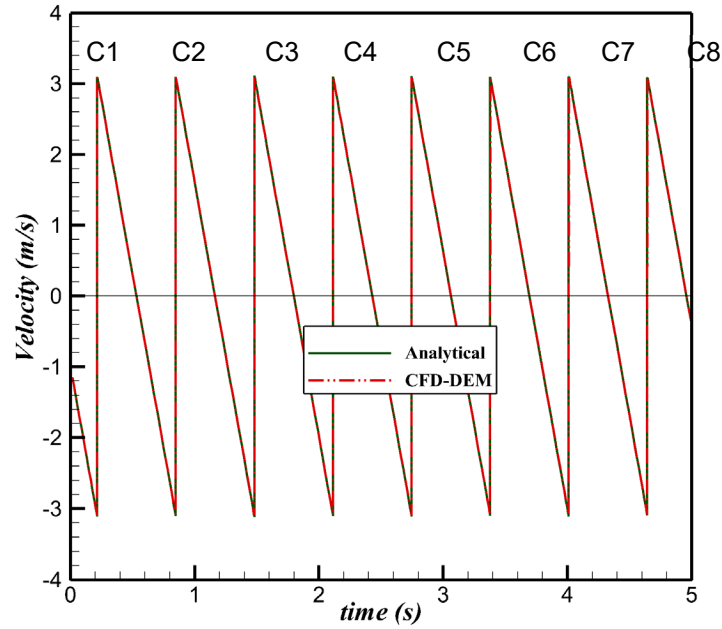
Figure 6.   CFD-predicted velocity compared to analytic results Equation (4), for the DEM sphere. *Points C1 through C8 represent collision events.*

In addition to instantaneous height and velocity, CFD-predicted impact velocity of the first collision incident and post-collision maximum height of the sphere are summarized in Table 2.

Table 2. Comparison of the CFD-predicted collision value with analytical value.

Collison Event	Analytical Value	CFD Prediction	
		Lagrangian Sphere	DEM Sphere
Impact Velocity (m/sec)	3.135	3.137	3.101
Post-collision maximum height (m)	0.501	0.50	0.495

2.2   Collision Detection; Sphere on Inclined Plate

This section extends the work for the collision detection method to a more complex system involving multiple dimensions in the absence of gravity. A sphere colliding with an inclined surface represents a two-dimensional elastic collision, including both direction and velocity changes. This setup more closely resembles the collision event that occurs in the hydropower unit, particularly the fish strike with the turbine runner blade. Like the previous section, the CFD-predicted impact velocities, collision points, and collision times were compared with corresponding analytical values.

2.2.1   Theoretical Derivation

Flow simulations were conducted to verify the collisions of particles with multiple surfaces. For this purpose, the collision of particles with an inclined plane (45° inclined to the horizontal) was considered in the absence of gravity. The collision event of the sphere was found to be two-dimensional, meaning the direction of the velocity changed after the collision. The sphere was released from a height h with an initial velocity u. The velocity of approach is constant due to the absence of the gravity. The sphere strikes the inclined plate and rebounds with a velocity v at an angle ϕ to the inclined plane. The schematic of the collision event for the inclined plane presented in Figure 7 delineates the components of pre- and post-collision velocity. The velocity of the sphere along the inclined plane does not change after collision. The relationship between the normal component of velocity of the sphere before and after collision can be expressed as follows:

$$v\sin\phi = -eu\cos\theta$$

(4)

Here, e is the coefficient of restitution ($0 \leq e \leq 1$) that accounts the energy loss associated with the collision event. For elastic collision, its value is unity, and subsequently Equation (5) leads to

$$v \sin \phi = -u \cos \theta \qquad (5)$$

For a smooth and frictionless surface, the component of velocity along the inclined plane does not change after collisions.

$$v \cos \phi = u \sin \theta \qquad (6)$$
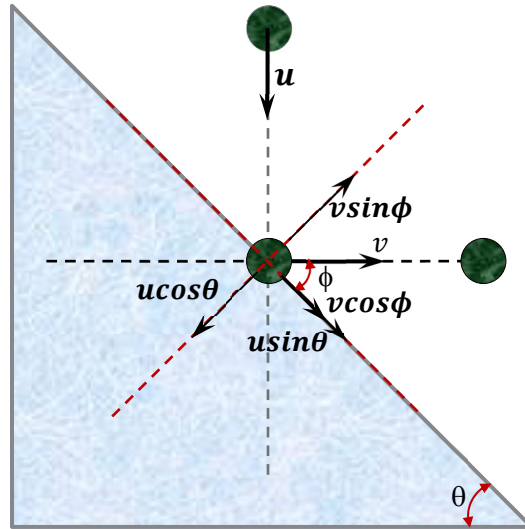
Figure 7.   Components of pre- and post-collision velocity. Plane is 45° inclined.

Solving Equations (6) and (6) for the value of $\theta = 45°$, the following value appears:

$$\phi = \theta = 45°$$
$$v = -u \qquad (7)$$

Equation (8) shows that an initially vertically falling sphere will move horizontally after collision with the inclined plane.

2.2.2   Computational Simulations

The CFD simulations were conducted for the computation of the trajectory and collisions of a sphere with multiple walls in the flow domain (Figure 8). In the simulation, external forces were not considered, and gravity was also turned off. The computational flow domain was filled with stagnant air as a primary phase in which the sphere moves down. It strikes the inclined bottom, subsequently colliding with the right-side wall and top face of the flow domain. Both Lagrangian and DEM simulations were independently performed to capture collision events. The sphere was released from a height $h \ (= 0.44 \, m)$ with initial velocity $u \ (= 1 \, m/sec)$. Figure 9(a) shows the collisions of the sphere with different solid walls of the flow domain. As seen in Figure 9(a), the sphere first collides (C1) with the inclined bottom at t = 0.34 sec. After collision, the sphere horizontally moves and hits the right wall (R1) in 0.44 s. The change in the direction can be understood from the Equation (7). The sphere bounces and re-hits (C2), the bottom, at 0.54 s due to the normal collision of the sphere with the right wall. Because of the perfect elastic collision with the 45° inclined plane, the sphere vertically moves in an upward direction. The upward motion of the sphere in the absence of gravity leads to another collision of the sphere

with the top (T1) at 1.20 s. Subsequently, the sphere rebounds vertically down and hits the bottom wall (C3), and collision occurrences periodically repeat. The trajectory of the sphere is shown in Figure 9(b). The time for various collisions was recorded using a JavaScript in the simulations.
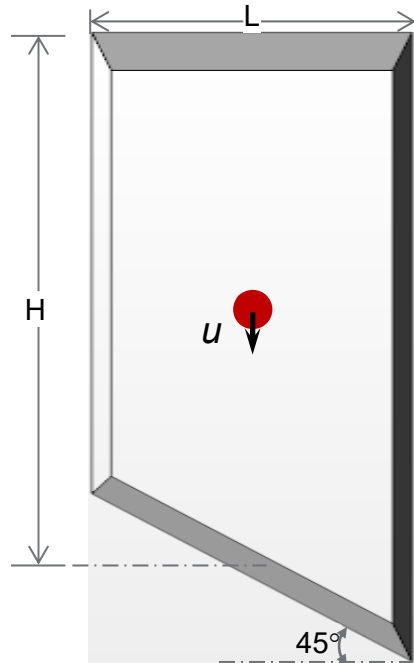
Figure 8. Schematic of flow domain showing initial position of sphere.
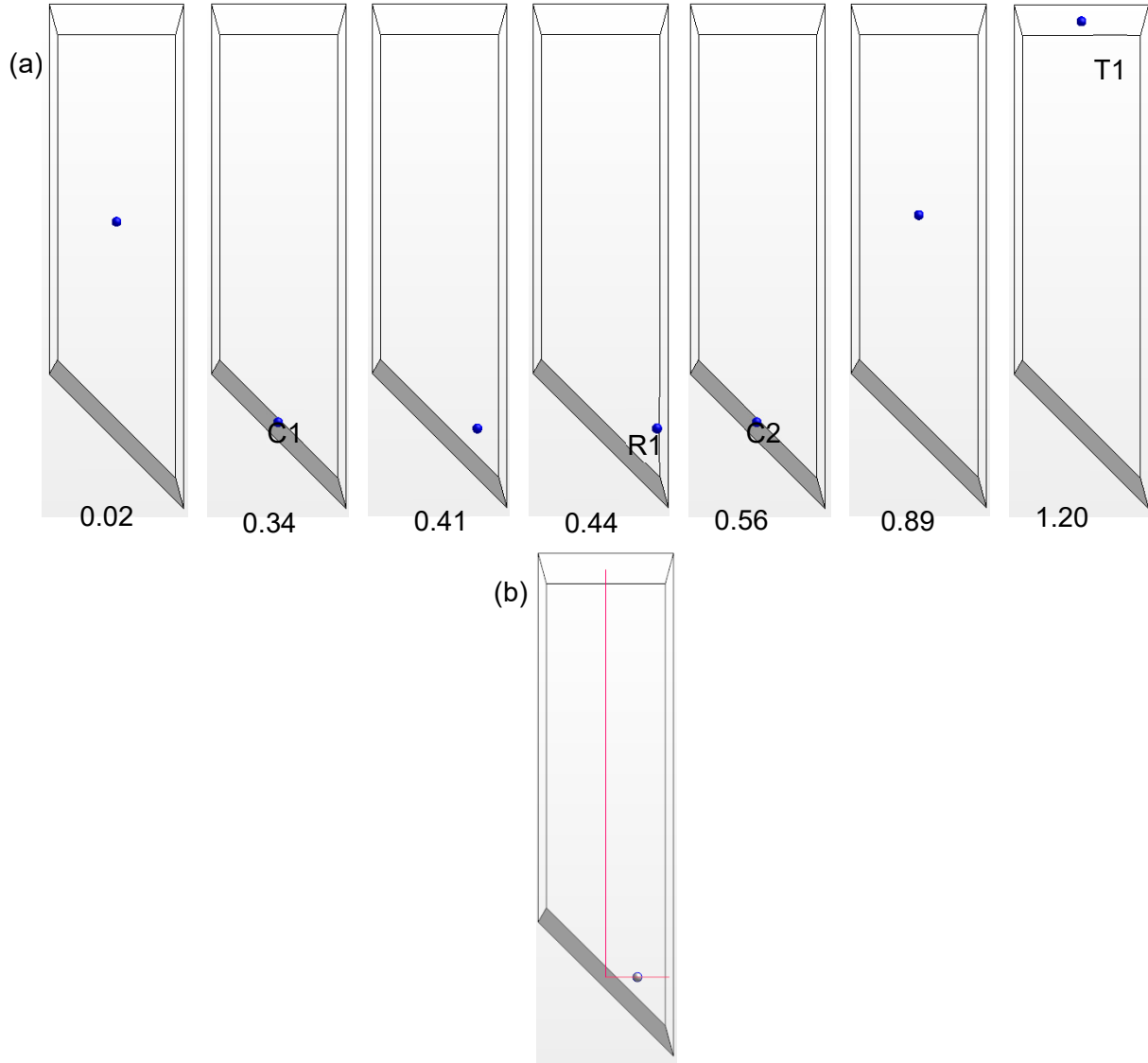
Figure 9. (a) Collision of the sphere with inclined plane and top/side walls; (b) Red line is path of sphere.

2.2.3 Timing for Collision Events

As mentioned above, the sphere strikes the bottom, right wall, and top of the flow domain periodically. Accordingly, the time for each collision event was computed separately. In the current case, the magnitude of the velocity does not change after the collision, but the collision alters the direction of the sphere. The time for the different collisions can be computed by a simple calculation, as follows:

    a. Inclined plane (C_i)

$$T_{n+1} = T_n + A_t$$

(9)

The term A_t depends on the direction of sphere velocity and computed as:

$$A_t = \begin{cases} (2H+L)/u & \text{for } u \neq 0 \\ L/v & \text{for } u = 0 \end{cases}$$

(10)

b. Right plane (R_i)

$$T_{n+1} = T_n + 2H/u + L/v$$

(11)

c. Top (T_i)

$$T_{n+1} = T_n + 2H/u + L/v$$

(12)

As shown in Table 3–Table 5, the CFD-predicted time for both types of particles matches well with the analytical values at each collision event. There is a slight discrepancy for the DEM particle, which might be due to the surface-to-surface contact in the DEM method, in contrast to the center-to-center contact found in the Lagrangian method.

Table 3. Comparison of CFD-predicted collision times with analytical values, inclined plane.

Collison Event	Analytical Value (sec)	CFD Prediction (sec)	
		DEM Sphere	Lagrangian Sphere
First (C1)	0.35	0.336	0.35
Second (C2)	0.55	0.516	0.55
Third (C3)	1.85	1.768	1.85
Fourth (C4)	2.05	1.947	2.05
Fifth (C5)	3.35	3.210	3.35
Sixth (C6)	3.55	3.369	3.55
Seventh (C7)	4.85	4.638	4.85
Eight (C8)	5.05	4.804	5.05
Ninth(C9)	6.35	6.066	6.35
Tenth (C10)	6.55	6.239	6.55
Eleventh (C11)	7.85	7.494	7.85
Twelfth (C12)	8.05	7.674	8.05

Table 4. Comparison of the CFD-predicted collision time with the analytical value, right wall.

Collison Event	Analytical Value (sec)	CFD Prediction (sec)	
		DEM Sphere	Lagrangian Sphere
First (S1)	0.45	0.423	0.45
Second (S2)	1.95	1.857	1.95
Third (S3)	3.45	3.289	3.45
Fourth (S4)	4.95	4.720	4.95
Fifth (C5)	6.45	6.152	6.45
Sixth (C6)	7.95	7.583	7.95
Seventh (C7)	9.45	9.015	9.45
Eight (C8)	10.45	10.445	10.45

Table 5. Comparison of the CFD-predicted collision time with an analytical value, top.

Collison Event	Analytical Value (sec)	CFD Prediction (sec)	
		DEM Sphere	Lagrangian Sphere
First (T1)	1.20	1.142	1.20
Second (T2)	2.70	2.573	2.70
Third (T3)	4.20	4.005	4.20
Fourth (T4)	5.70	5.436	5.70
Fifth (T5)	7.20	6.868	7.20
Sixth (T6)	8.70	8.299	8.70
Seventh (T7)	10.20	9.730	10.20

Next, the CFD-predicted velocity of the sphere was compared with the analytical value. Figure 10 shows that the CFD-predicted velocity computed by both methods excellently matched the analytical value in both directions.
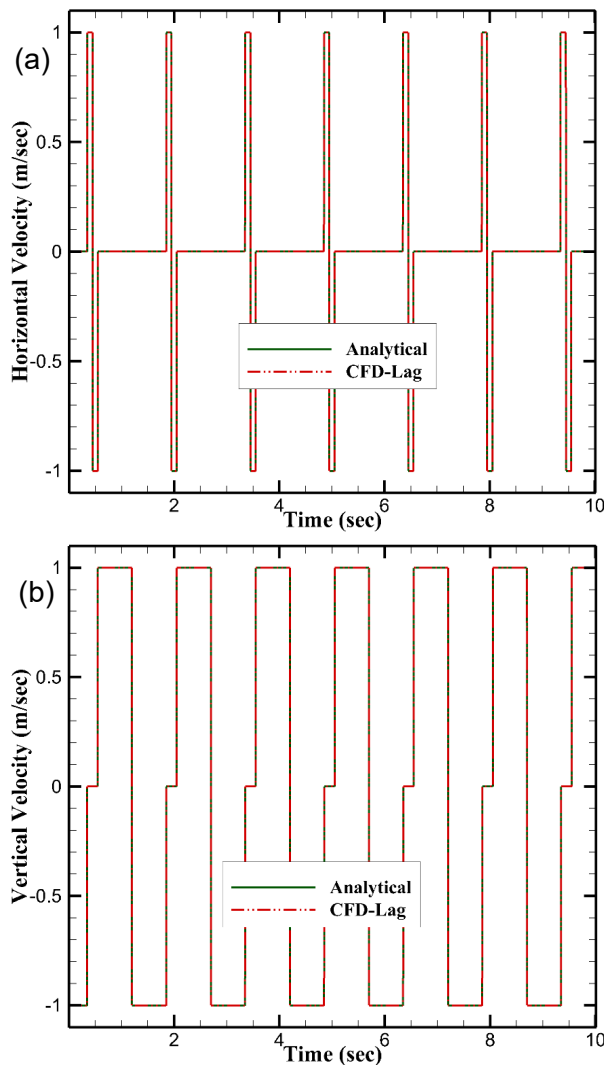
Figure 10. CFD-predicted velocity compared to analytic value of Lagrangian sphere: (a) horizontal velocity, and (b) vertical velocity.

The CFD-predicted instantaneous position of the sphere compared well with the analytical value in both directions as shown in Figure 11.
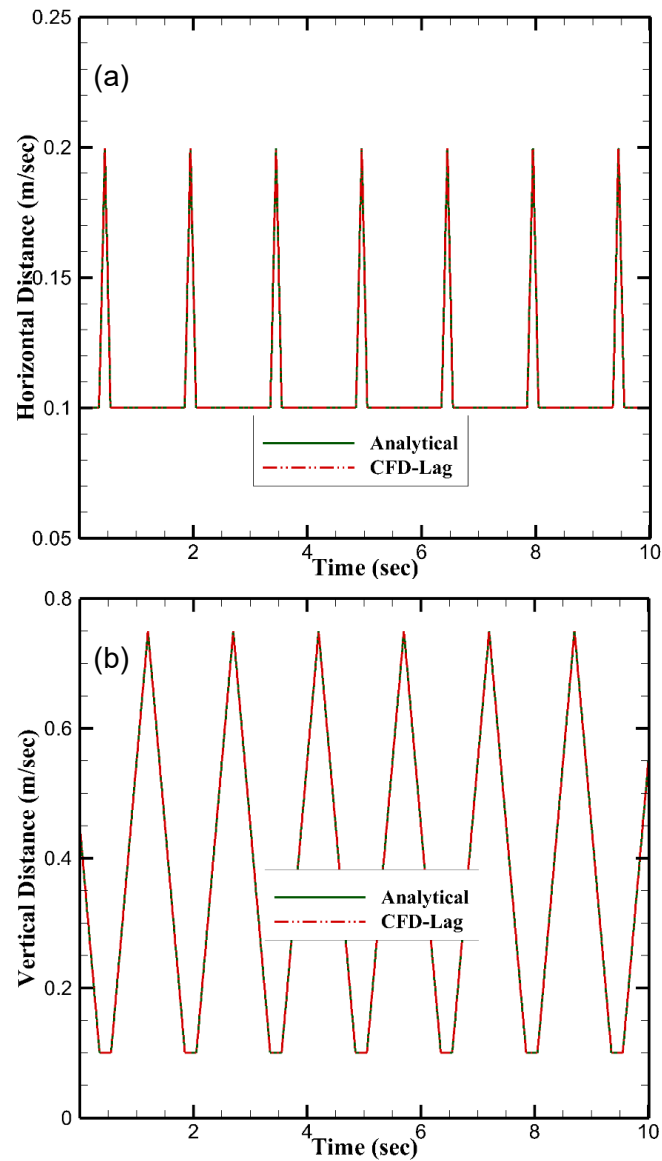
Figure 11. CFD-predicted positions with analytic value of Lagrangian sphere: (a) horizontal and (b) vertical directions.

In addition to temporal position and velocity, the CFD-predicted impact velocities of the first collision at various planes also compared well and are summarized in Table 6.

Table 6. Comparison of CFD-predicted impact velocity with analytic value at the first collision.

| Surface | Analytical Value (m/sec) | | CFD Prediction (m/sec) | | | |
| | | | DEM | | Lagrangian | |
	x velocity	z velocity	x velocity	z velocity	x velocity	z velocity
Bottom	0	-1.00	0	-1.00	0	-1.00
Right	1.00	0	1.00	0	1.00	0
Top	0	1.00	0	1.00	0	1.00

In conclusion, the present method of detecting the collision of particles with solid surfaces in the CFD simulation is successfully validated. This method can be employed for collision data extraction in the CFD simulations as input for the BioPA toolset.

3. Particle Striking Validation for CFD Models

3.1 Particles Striking Vane Arrays

Particles striking the vane array were studies to explore the influence of flow field on the particle collision rate in an idealized hydropower turbine distributor, consisting of stay vanes and guide vanes (wicket gates) in a flume with linear flow. The design of the vane array is identical to the experimental test of the idealized distributor of the Kaplan turbines operating at Ice Harbor Dam, located on the lower Snake River in Washington State. Preliminary flow simulations were conducted to validate the flow field prediction and particle collisions. An extensive CFD simulation campaign was performed to validate the velocity distribution upstream and downstream of the vane array and the particle collision rate with the previously performed experimental results of Harding et al. (2019). Note that the flow field significantly affects the particle trajectory at low particle inertia. Therefore, CFD-predicted velocity profiles at different axial locations in the flume were compared with experimental results.

3.1.1 Model Setup and Meshing

The computation model of the flow domain is the same as that used in the experimental studies of Harding et al. (2019). The dimensions of the stay vanes and guide vanes, also called wicket gates, were determined using Froude scaling by a factor of 1/12. For the sake of brevity, the experimental design is not presented here, but the details are described by Harding et al. (2019). The vane array and injection tube were inserted in a rectangular flume whose dimensions were $3.5 \times 0.89 \times 0.53 \ m^3$ (see Figure 12). The angular configuration of the stay and guide vanes analyzed was the lower 1% turbine operating condition at Ice Harbor Dam. The lower 1% operating condition corresponds to the lowest flow rate to achieve a turbine efficiency within 1% of the peak efficiency for a given head. The injection tube (diameter = 16 mm) was placed at the center of the domain, and neutrally buoyant particles were injected in the flow domain through the outlet of the injection tube. The injected particles are spheres (diameter = 3.6 mm) and cylinders (diameter = 2.0 mm and length = 8 mm).
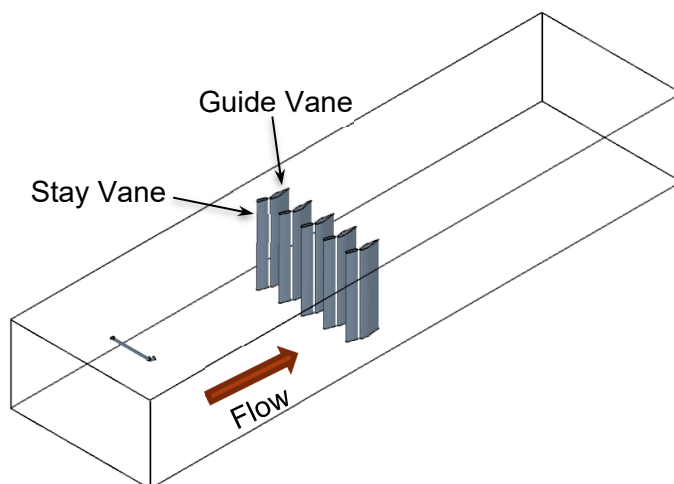

Figure 12. Computational flow domain showing vane array.

The model of the computational flow domain was created in Solidworks, a commercial computer-aided design (CAD) software, as shown in Figure 12. Subsequently, the CAD model

of the flow domain was imported into the commercial CFD code Star-CCM+ (Siemens PLM Software) for meshing and flow simulations. To capture the hydrodynamics and impaction of particles with the vane array accurately and efficiently, the computational flow domain was discretized with nonuniform trimmed mesh, shown in Figure 13. Note that the trajectory of a neutrally buoyant particle follows the path of the existing flow field at a lower value of particle inertia. As shown in the exploded view of the mesh in Figure 13, the mesh near the stay and guide vanes was created using prism layer mesh (same as boundary layer mesh in other CFD software). In this region, wake and flow recirculation can be expected; consequently, a very fine mesh (size on the order of *millimeters* shown as a very dark region in Figure 13) is required to capture flow behavior. The central region near the injection tube was refined to capture the hydrodynamics and particle trajectory accurately. A gradient-based trimmed mesh was used to discretize the remaining parts of the flow domain. The grid convergence test was performed relative to the variation in velocity profiles at different axial locations and particle collision rates with the vane array. For the sake of brevity, the results of the grid convergence test are not presented here.
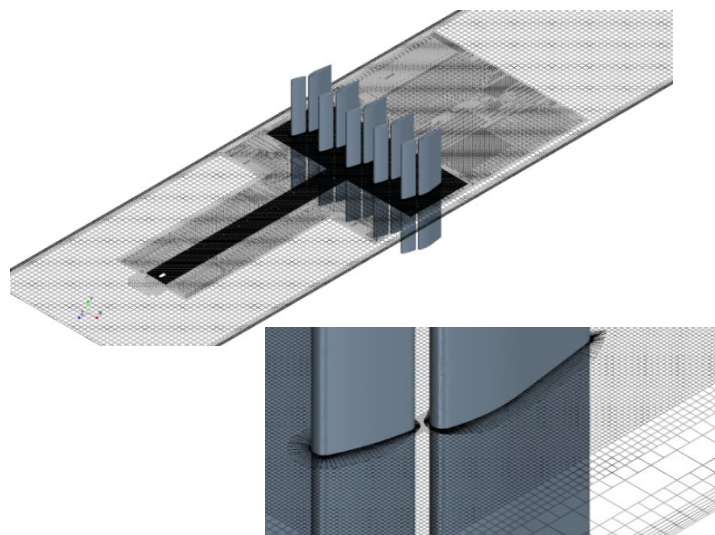
Figure 13. Meshing scheme used. Note fine mesh near vane to capture flow.

The unsteady turbulent multiphase flow simulations were conducted using Star-CCM+ (Siemens PLM 2017). The shear stress transport (SST) k-ω model, which is an appropriate turbulence model for capturing turbulent wake and flow, was selected in the simulation. The multiphase flow simulations were conducted using the Euler-Lagrangian approach, which is widely adopted for modeling particulate flow. It involves the tracking of particles within the Eulerian phase. Lagrangian particle tracking was used for computing the particle trajectories and the particles' collisions with the vane arrays. The other approach—DEM—is a soft particle method that can efficiently provide insight into phenomena that occur during the collision of particles. The DEM model extends the Lagrangian approach, accounting for inter-particle interaction in the equations of motion. It allows overlap between particles and accounts for the surface contact force. Therefore, the DEM method was selected, because it is more suitable for use in the current flow simulation of particle collisions in a hydropower unit.

In line with the experiments, flow simulations were conducted at two inlet velocities (0.26 and 0.53 m/sec). The particle's trajectory and its collision with the vane array were computed at both flow rates. The particle's collision with the vane array was detected in the simulation using a user-defined JavaScript function. The script captures the desired data associated with particle's

index during collisions. Water was used as the working fluid. Neutrally buoyant spherical and cylindrical beads were chosen. The details of the experimental setup and results are described by Harding et al. (2019). The uniform velocity and pressure outlet boundary conditions were specified at the inlet and outlet of the flow domain. The side wall, vane array, and wall of the injection tube were specified as a no-slip boundary condition.

3.1.2 Comparison of Predicted and Experimental Results

The results of the flow simulations were analyzed in terms of the velocity profiles and the collision of particles with the vane array. Note that the flow field significantly affects the particle dispersion and collision. Hence, it also needs to be validated. Figure 14 shows a snapshot of the velocity field at the horizontal plane located at the center of the flow domain. The downstream vortex and flow reversal in the vane array region are clearly visible. In addition, the injection tube creates a wake affecting the particles' trajectory.
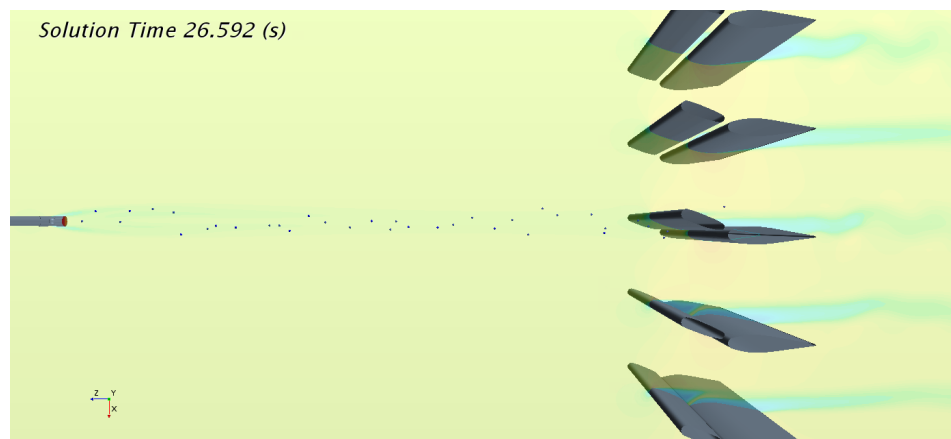
Figure 14. Velocity contours, collisions, and dispersion of small suspended spherical particles. Note wakes and flow reversal due to vane array and injection tube.

The CFD simulation results were compared with the experimental results for the velocity profile at different axial locations upstream and downstream from the vane array. Consistent with the experimental studies, the axial velocity profiles were computed at corresponding locations in the flow domain. The position of these locations is presented in Figure 15. The axial velocity (U) was normalized by the upstream velocity (U_0) as U/U_0. The lateral position (W) was also normalized by separation between consecutive vanes (G) as W/G. The velocity at the upstream location (10U) shows the influence of upstream wake generated by the stay vane. The interaction between the downstream wake caused by the injection tube and upstream wake caused by the stay vane leads to a complex flow structure. This flow field substantially affects the upstream dispersion of the particles as well as their collision with the vane array.

Note that the experimental measurement might have a small data sample and measuring points are limited. CFD can resolve a small spatial resolution at all locations and it can capture small-scale flow characteristics that were not captured in the experimental studies. Reasonably good agreement was obtained between both results.
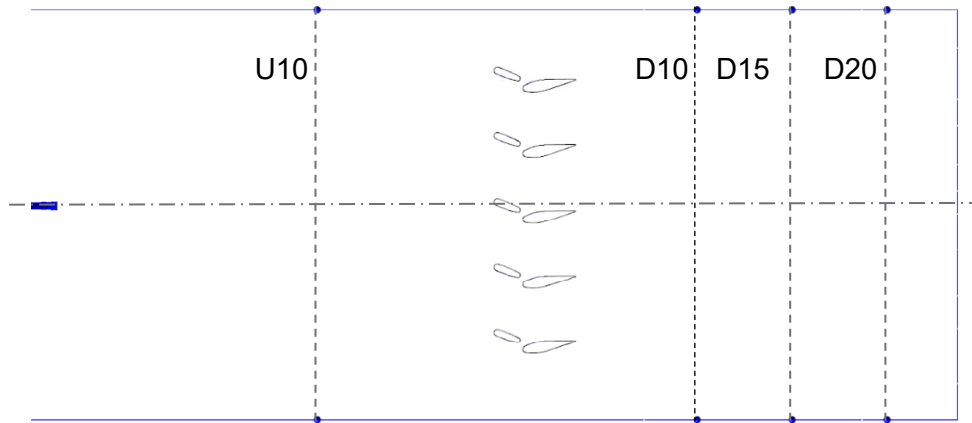
Figure 15. Locations of velocity measurement for comparison of the CFD-predicted results (D = downstream, and U = upstream).
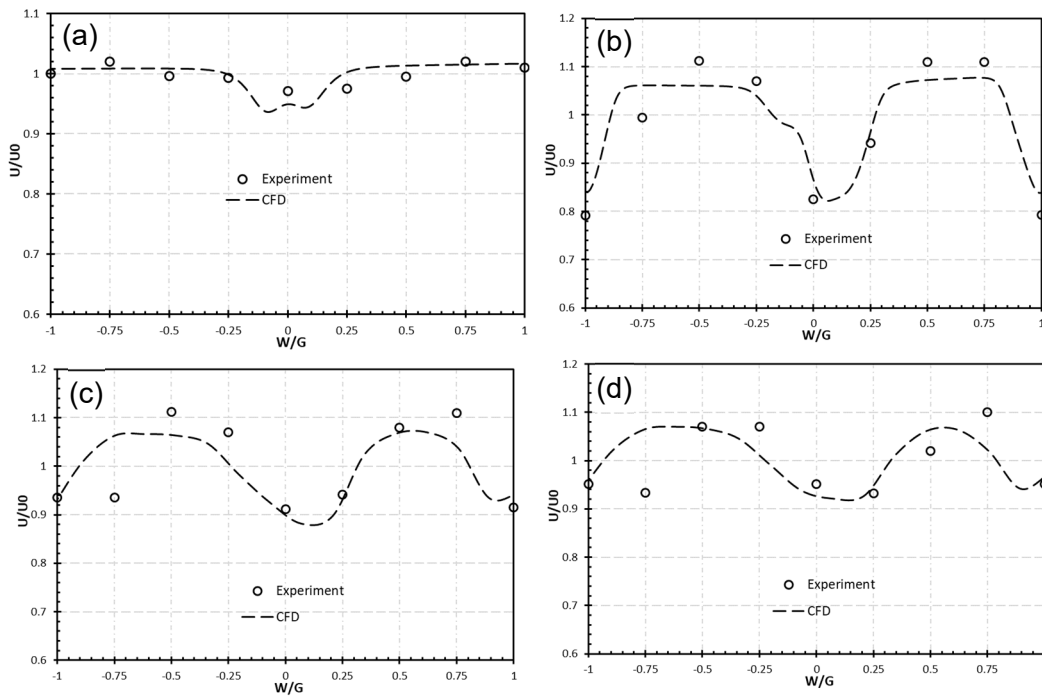
Figure 16. Comparison CFD-predicted velocity with experimental data in the flume at U0 = 0.53 m/sec. Locations (a) 10D upstream (U10), (b) 10D downstream, (c) 15D downstream, and (d) 20D downstream. Positions shown in Figure 15.

Next, CFD-predicted particle collisions rates were computed. The collision of the particle was detected via boundary sampling during the simulation, see Figure 17a. The boundary sampling does not create a file that stores all data corresponding to a particle during collision. A JavaScript function was developed that automatically saves the sampling data into the file during every collision event. Because of the flow reversal and wake proximity to the vane array, a particle can collide multiple times with vane arrays, and the JavaScript generates a separate file for each collision event. A similar phenomenon was also observed in the experiment conducted by Harding et al. (2019). The number of stored files does not reflect the actual value of colliding particles. Subsequently, the output files generated during every collision need further

analysis to accurately count the number of particles colliding with the vane array. The stored files during each collision event were analyzed in MATLAB, and the actual number of collided particles was computed. The CFD-predicted collision of the particles was compared with the corresponding experimental value of both flow rates. The collision rate was presented as the percentage of the released particles that struck the vane array. In Figure 17b and c, it can be clearly seen that the CFD-predicted collision rate lies within the upper and lower limit of experimental observation for particles and flow rates. In the experimental observation, the upper and lower limit of the collision rate was provided according to sample size. After achieving good agreement between results, we conclude that the present method of flow simulation for particle collision is validated and can be used for further predictions in complex systems.
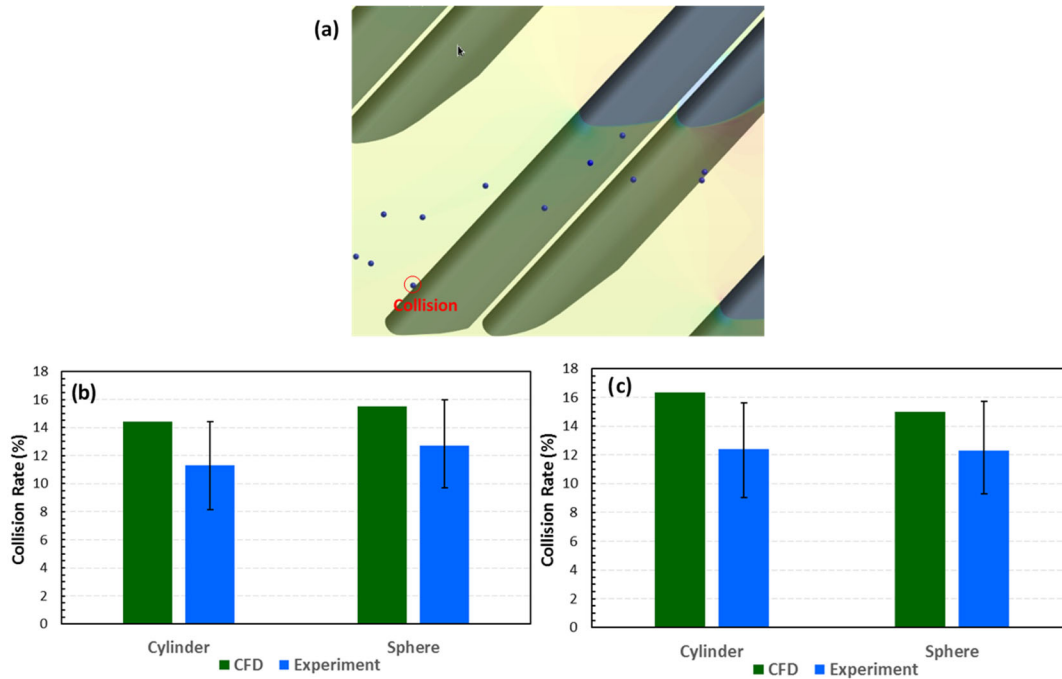

Figure 17. (a) Region near vane array. Dispersion in flow and collision with vane array shown. Graphs comparing collision rate of particles and vane array at flow rates of (b) Re = 10,000 and (c) Re = 20,000.

3.2 Particles Striking a Cylinder

Preliminary flow simulations for the collision of particles with a circular cylinder (target) were conducted. They demonstrated the impacts of flow field on the collisions and dispersions. Note that a particle follows the path of the existing streamtrace in the flow field at the small value of particle inertia. CFD simulations for the prediction of particle collision with a cylindrical body were validated against the experimental results of Harding et al. (2019). Cylinders were selected as they are the most simplistic shape for CFD validation. Neutrally buoyant spherical particles were injected into the water flume, and the collision of the particles with the cylinder was detected using a high-speed camera (see Figure 18). Accordingly, CFD simulations were conducted to compute the dispersion and collision of the particles at two flow rates. The results were quantified and compared with the experimental observations.
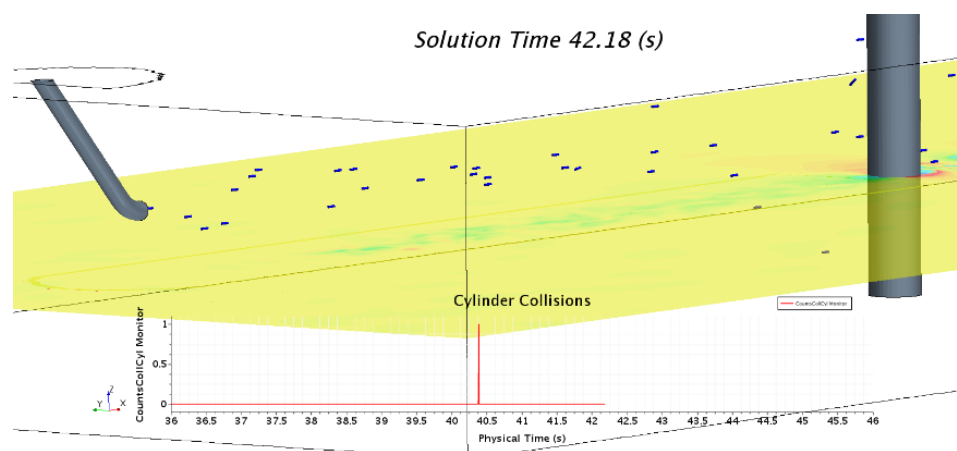
Figure 18. Cylinder and injection tube in flow domain. Flow field, suspended particles, and collision detection in the flow simulation are shown.

3.2.1 Problem Setup and Meshing

The CFD investigations of the flow around a cylinder were conducted using a commercial CFD code Star-CCM+ (Siemens PLM Software). The three-dimensional (3-D) model of the computational flow domain was developed according to the experimental model of the flume. The flow model consists of a rectangular domain having dimensions of 80D×24D×2πD, where D is the diameter of the cylinder. The inlet and outlet of the flow domain was located 30D upstream and 50D downstream from the cylinder. Further details of the computational models and setup are described by Romero-Gomez et al. (*In Press*). The spherical particles were injected at 23.7D upstream from the cylinder.

As shown in Figure 19, the flow domain was discretized with nonuniform hexahedral mesh according to local flow characteristics in the flow domain. Near the cylinder wall, prism layer (boundary layer) meshing was used to resolve the boundary layer growth. In this region, a higher strain rate is expected. In addition, the flow region near the cylinder was refined to capture the wake and flow reversal. The remaining parts of the flow domain were meshed with relatively coarse mesh that featured a gradual increase in the cell size. A grid sensitivity test was performed to optimize the number of cells (~ 10 millions) in the flow simulation. For the sake of brevity, details of this test are not presented here.
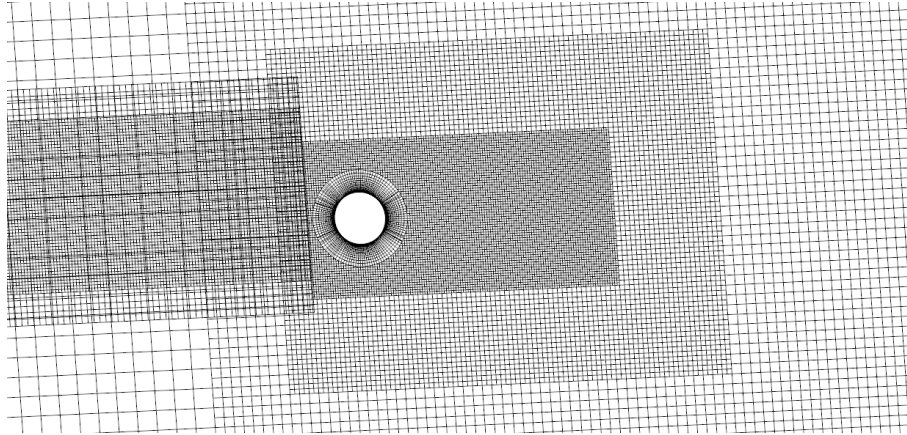
Figure 19. Meshing of the computational flow domain. Note nonuniform mesh to capture wake and flow circulation.

Unsteady turbulent multiphase flow simulations were conducted using the Detached Eddy Simulation version of the SST k-ω turbulence model. To track the particle motion, a Euler-Lagrangian multiphase approach was chosen. The SST k-ω model is an appropriate turbulence model for capturing existing complex flow behavior such as wake and flow reversal. In line with experimental conditions, flow simulations were conducted at two flow rates. The particle's trajectory and the collision of the particle with the cylinder were simulated for both cases. The collision detection was performed using JavaScript, which enabled the recording of data of interest. After the simulations were converged, post-processing of the data was conducted to analyze the particle collisions and dispersion according to experimental conditions. The results were analyzed in terms of Reynolds number ($\mathrm{Re} = U_0 D/\nu$, where U_0 is flow velocity, D is the diameter of target cylinder, and ν is the kinematic viscosity of the liquid). Reynolds number is a dimensionless number used to represent fluid inertia. Water was used as the working fluid and neutrally buoyant spherical beads were selected. Details of the experimental results and data are described in (Harding et al. 2019). The test conditions for the CFD simulation and experimental conditions are presented in Table 7.

Table 7. Simulated test conditions.

Test Case	$\mathrm{Re} = U_0 D/\nu$	Release Location from Center
1	10,972,	0
2	22,366,	0
3	10,972,	0.5D
4	22,366,	0.5D

3.2.2   Comparison with Experimental Results

The lateral dispersion of the spherical particle at 2D upstream of the cylinder is presented in Figure 20 for both Reynolds numbers. It can be seen clearly that both methods (CFD simulations and experiments) show identical trends. There is little discrepancy in the peak value of the dispersion curve and the sharp peak at the center is not found in both Re values. Further, the increased value of the flow rate leads to wide dispersion of the particles. This deviation is linked to the travel time; that is, by the time spheres arrived at the measuring location, they had

had a greater travel time for dispersing at the low Reynolds number than at the high Re value. Note that the spheres were not released from a single point at the center of a tube exit. Instead, they were released from an array of points at the exit of injection tube.
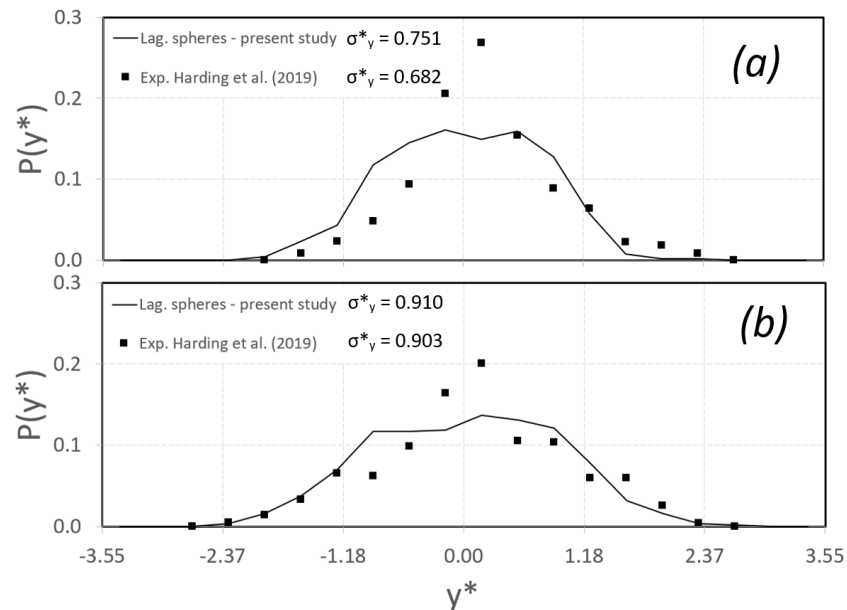

Figure 20. Comparison of CFD and experimental (Harding et al. 2019) dispersions of spherical particles 2 diameters upstream of cylinder; (a) Re = 10,972 and (b) Re = 22,366.

Next, the collision of the spherical particles with the target circular cylinder was computed. The percentage of collisions was computed as the ratio of the collided particles and the total number of injected particles. Figure 21 shows the comparison of the CFD-predicted and experimentally measured percentage collision of spherical particles with cylinders. The CFD prediction of particle collision with circular cylinders is in a good agreement with the experimental condition and both show almost the same frequency of occurrence. The rate of collision was lower for releases in the offset location than for releases at the centerline. The influence of the fluid velocity on the collision rates depended on the release location; for centerline releases (Tests 1 and 2), higher Re yielded lower collision rates, but this trend was reversed for the offset releases (Tests 3 and 4). In the CFD simulation, the numbers of sphere-cylinder interactions were counted as collision events and recorded as the modeled rate of collision. In the experiments, the collisions between the sphere and cylinder were visually observed. A small discrepancy between both approaches was observed, but the predicted collision frequency was within acceptable limits. Therefore, the current method of CFD simulation for particle collision can accurately predict the flow behavior.
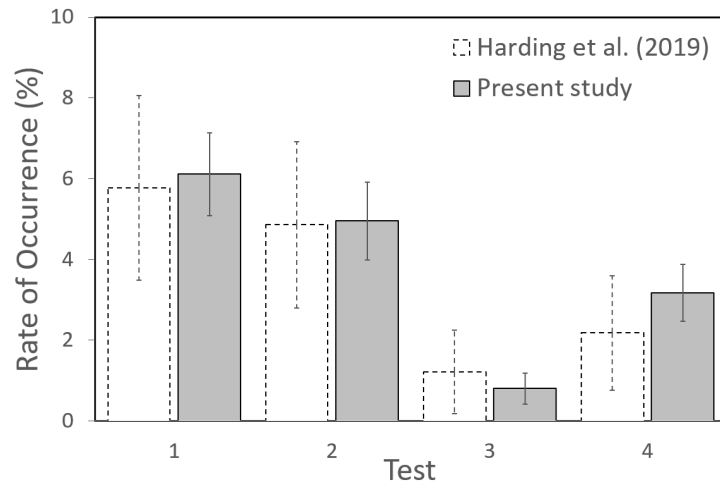
Figure 21. Percentage collision rate of spheres with circular cylinder.

4. Characterization of Flow through Hydraulic Turbines

4.1 CFD Modeling for a Francis Turbine

The studies of the biological performance assessment of hydropower turbine units have largely been associated with Kaplan turbines installed at low-head hydropower facilities in the Columbia River (e.g., Richmond et al. 2014b). In comparison, the Francis turbine is very prevalent throughout the country, because it can operate over a large range of discharges and heads. This section is focused on applying the BioPA toolset to assess the ecological impact of the Francis turbine. Before applying the BioPA toolset, one needs to validate the flow characteristics of the Francis turbine. In this context, the Francis-99 turbine and available case studies by the Norwegian University of Science and Technology (NTNU) have been chosen for flow investigation. In this study, hazardous flow conditions for the model Francis turbine were characterized.

4.1.1 Data Set

The NTNU research team played an active role in providing data in the open literature about the Francis-99 turbine. Laboratory-scale results were provided for the 1:5.1 scale model of the Francis turbine installed at the Tokke station unit in Telemark, Norway. The team provided the model's geometry, test conditions, and data for the pressure and velocities within the runner and draft tube. Results at three characteristic operating conditions (part load [PL], best efficiency point [BEP], and high load (HL)) have been reported. These data sets were used to validate the CFD predictions for the Francis turbine and as the input for the current version of the BioPA toolset.

4.1.2 Problem Setup and Meshing

The flow-through Francis-99 model for comparison to CFD-predicted results with laboratory data under three operating conditions (PL, BEP, and HL) was investigated. Two recent modeling enhancements for biological performance assessment were implemented: (1) the use of Lagrangian particles to quantify the collision rates and conditions on the stay vanes and the runner, and (2) the actual motion of the runner as particles pass the rotating region. The physical model has been tested and analyzed in a laboratory setting at the NTNU and reported in a series in regular workshops. The contributions from participants were reported at the second Francis-99 workshop in 2016, and they focused on examining the flow fields at three operating conditions.

The Francis-99 geometric model details are accessible online for testing and validating the accuracy of the numerical prediction of the flow-through Francis turbine (NTNU 2016). The geometric model consists of the spiral casing, stay vanes, guide vane (wicket gates), runner, draft cone, and draft tube geometry for each of the three operating conditions. The guide vane pitch is dependent on the operating condition; the other regions and features remain fixed. The CFD modeling for the flow and performance characteristics of the Francis turbine is conducted in a manner similar to that of Casartelli et al. (2017).

The CAD file in parasolid format of the different components of the Francis-99 model was imported in Star-CCM+ to create the computational flow models (Figure 22). The design and operating conditions of Francis-99 turbine were the same as the data provided by NTNU for the Francis-99 turbine. Geometric models for the three configurations were divided into the intake,

the distributor, the runner, the draft cone, and the draft tube. The various components of the turbine assembly were connected through the interface. The computational flow domain was discretized using an automated meshing scheme with a prism layer and nonuniform mesh (see Figure 23a). The automated scheme was capable of locally refining the mesh according to the requirements of the topology. The flow regions near the stay vanes, wicket gate (guide vanes), and runner have more refined cells (see Figure 23b). The runner blade and remaining wall of the flow domain were meshed with a prism layer meshing scheme to capture the steep flow gradient.
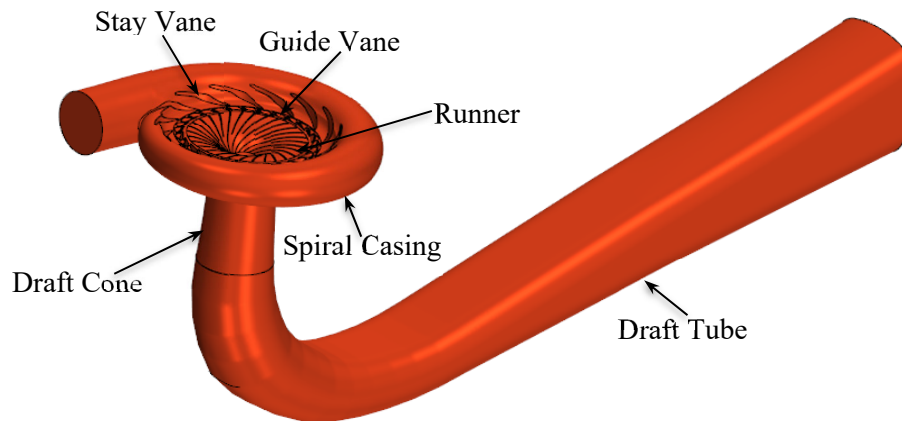

Figure 22. Computational model of Francis turbine unit.
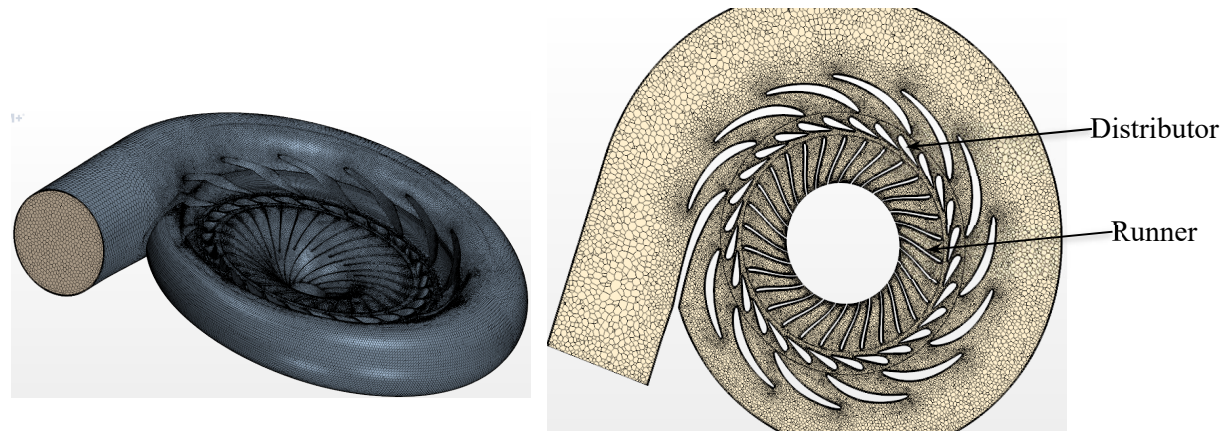
Figure 23. (a) Computational flow domain mesh, and (b) a horizontal cross section showing refined mesh in runner and distributor regions.

The adequate grid resolution in the prism layer was further varied from the y^+ value, a dimensionless distance, to measure the wall distance. The value of y^+ was found to be low enough to accurately capture flow characteristics. The optimum number of cells was arrived at after conducting a grid independency test. For the sake of brevity, the results of the grid independency test are not presented here. The overall number of cells in the flow simulations was found be on the order of 14–16 million.

Transient flow simulations were conducted using the multiple reference frame (MRF) method to evaluate the performance and flow characteristics in the Francis turbine assembly under different operating conditions. The flow region of the runner was specified to be the rotating region according to the prescribed rate in Table 8. Remaining regions, such as those of the

spiral casing, wicket gate, draft cone, and draft tube, were specified as the stationary region. The circumferential mixing condition was specified for the interface between the rotating and stationary regions (runner/distributor and runner/draft cone). The remaining interfaces were specified as direct interfaces. The Francis-99 website (see Table 8) provided the input data used in the flow simulations. The turbulent flow simulations were conducted using the SST k-ω turbulence model, which is widely accepted in the current setup of flow simulations. The liquid flow rate corresponding to the measured discharge was specified at the inlet, and the hydrostatic head was prescribed at the outlet of the draft tube according to values specified in Table 8. The remaining parts of the flow domain were specified as being a no-slip wall boundary condition. The flow simulations were conducted at the PNNL institution computer (PIC) cluster facility using 192 cores. Because of the transient nature of flow, flow simulations were conducted for up to 30 seconds physical time. The flow simulation nearly achieved steady state.

Table 8. Simulation parameters under different Francis-99 operating conditions.

Parameter	PL	BEP	HL
Guide vane angle (°)	6.72	9.84	12.43
Net head (m)	11.87	11.94	11.88
Discharge (m³ s⁻¹)	0.1396	0.1996	0.2425
Runner angular speed (rpm)	332.84	332.59	332.59
Hydraulic efficiency (%)	90.13	92.39	91.71

4.1.3   Comparison of the CFD and Experimental Results

The output data of the CFD simulations were analyzed for velocity, head loss, hydraulic efficiency, torque, etc. The currently predicted results were compared with experimental results and other independent CFD simulations by Casartelli et al. (2017). These quantities evaluate the hydraulic performance of the turbine unit, which can significantly affect the biological performance calculation.

Figure 24 shows the location of the particle image velocimetry measurements that were used to validate the CFD-predicted velocity profile under three operating conditions. The velocity profile computed at these locations was further compared with the experimental results and numerical predictions of Casartelli et al. (2017). Figure 25–Figure 27 show the comparison of the CFD-predicted results with experimental and numerical results by Casartelli et al. (2017). The CFD-predicted velocity profiles matched excellently for the BEP and HL conditions. A discrepancy in the velocity profile was found in the core region for the PL condition when comparing CFD to experimental results. This is likely due to development of a coherent vortex rope structure in the draft cone, likely creating uncertainty in the experimental measurements. Away from the core vortex rope, the CFD-predicted results matched very well with experimental results. Indeed, for the independent simulation in the same group, Casartelli et al. (2017) also found similar difficulty in comparing the velocity profile in this region. Overall, the predicted velocity profile excellently matched CFD-predicted results.
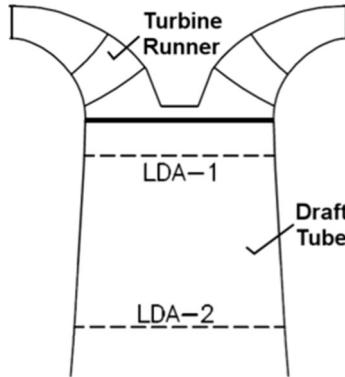
Figure 24. Position of the velocity-measuring locations in the draft cone under three operating
conditions.
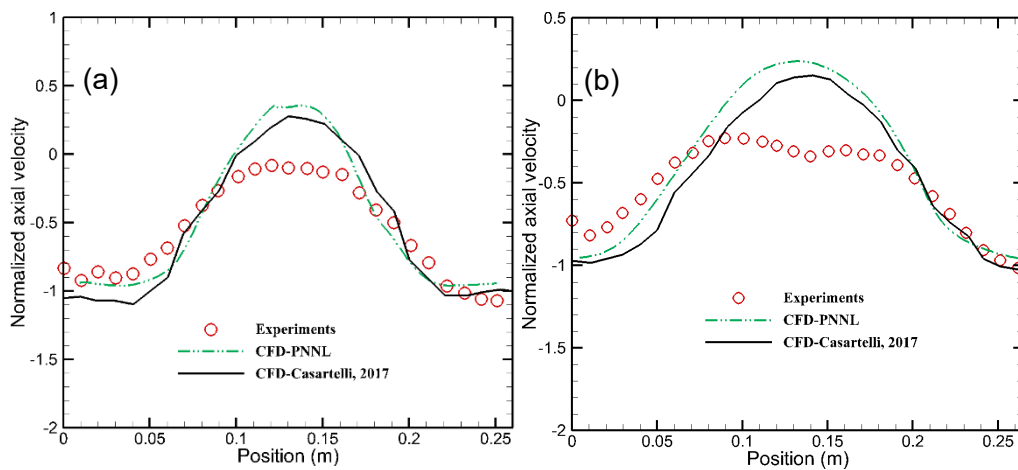
Figure 25. Comparison of the axial velocity profiles for the PL condition at (a) LDA-1 and (b)
LDA-2. Positive values are down relative to runner.
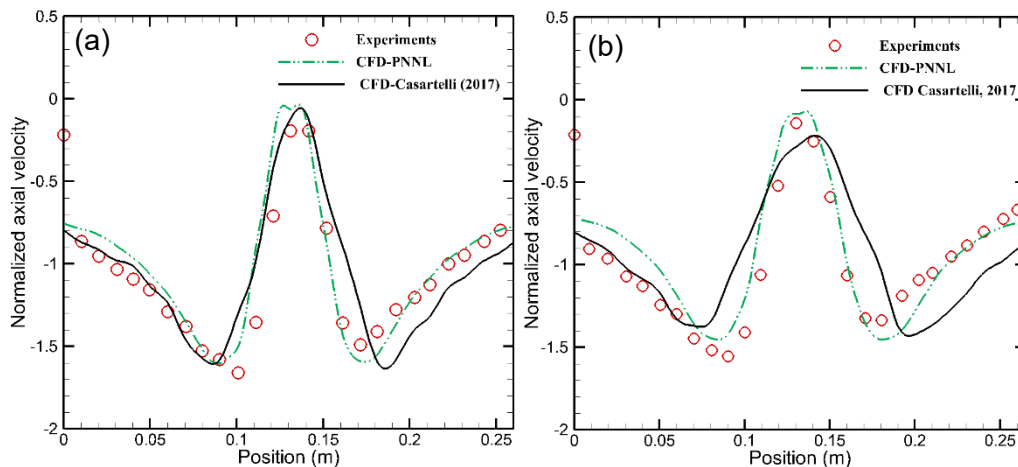

Figure 26. Comparison of the axial velocity profiles for the BEP condition at (a) LDA-1 and (b)
LDA-2.
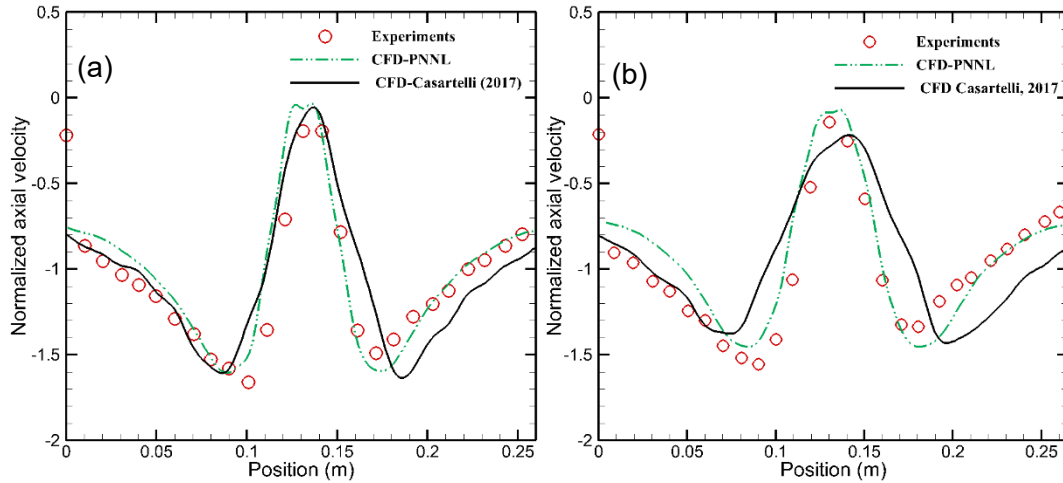
Figure 27. Comparison of the axial velocity profiles for the HL condition at (a) LDA-1 and (b) LDA-2.

Next, pressures in the turbine were compared for the locations shown, see Figure 29
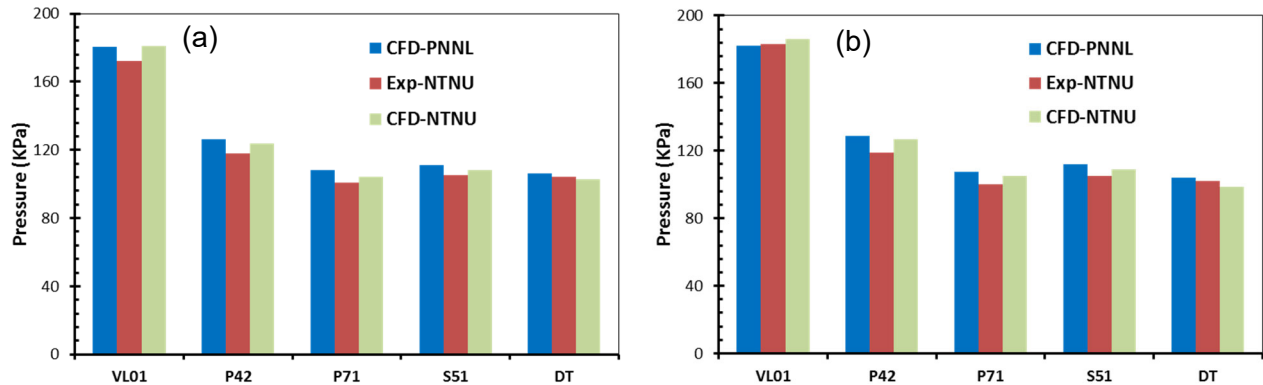
Figure 28. Comparison of CFD-predicted pressure with corresponding experimental observed pressures.
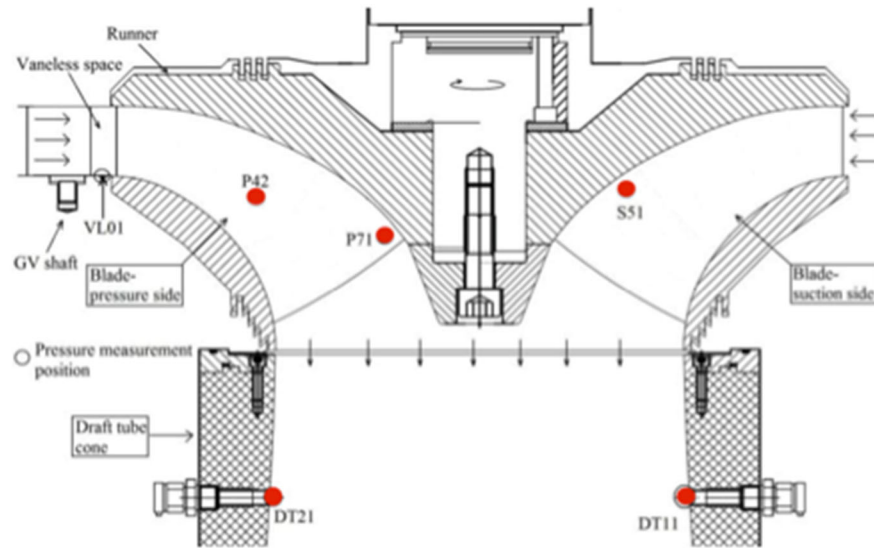
Figure 29. Position of pressure sensors under three operating conditions. VL01: vaneless space; P42: blade pressure side; P71: blade pressure at trailing edge; S51: blade in suction side; DT: draft cone.
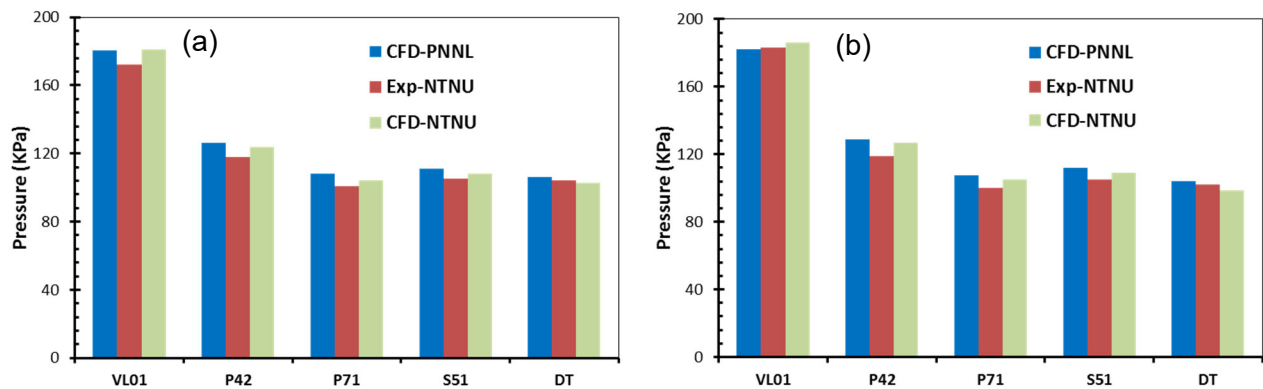
Figure 30. Comparison of total pressure at different locations for the (a) BEP and (b) HL operating conditions.

The outcome of the CFD simulation was compared to hydraulic qualities such as torque, net head, and hydraulic efficiency. Results are shown in Table 9–Table 11. The CFD-predicted results are slightly higher, within 5%, of the experimental results. Further, the present CFD prediction excellently matched the numerical prediction by Casartelli et al. (2017).

Table 9. Comparison of the net head.

Load	Experiment	CFD	
		PNNL	Casartelli (2017)
HL	11.88	11.99	12.40
BEP	11.94	12.20	12.50
PL	11.87	12.32	12.50

Table 10. Comparison of the torque.

Load	Experiment	CFD	
		PNNL	Casartelli (2017)
HL	740.54	791.71	800
BEP	616.13	668.03	667
PL	416.39	460.60	462

Table 11.   Comparison of the hydraulic efficiency.

Load	Experiment	CFD	
		PNNL	Casartelli (2017)
HL	91.71	96.20	93.9
BEP	92.39	96.90	95.6
PL	90.13	94.66	94.2

The CFD-predicted results obtained during this study indicate an acceptable prediction of the flow conditions. The CFD-predicted flow conditions can be used in the BioPA toolset calculations of the turbine unit at the prototype scale. The results demonstrate the application of the BioPA toolset to a Francis turbine by comparing laboratory-measured velocities and pressures to those simulated in our CFD models. The successful validation of flow simulations will also facilitate characterization of general differences between Francis and Kaplan turbines with respect to biological response through the simulation of a full-scale prototype of the Francis turbine. In addition, the current simulations will aid in identifying changes to the BioPA toolset that may be needed for application to Francis turbines.

4.2 CFD Modeling for a Kaplan Turbine

To validate the CFD modeling method, simulations were conducted in the existing turbine runner design of the Kaplan turbine at McNary Dam (MCN) on the Columbia River in 2018. A similar turbine design is found throughout the Lower Columbia and Lower Snake River Dams. The existing geometric design of the turbine was used to create a CFD model of the hydraulic environment. Details of the CFD methods, operating points, and model configuration are described by Serkowski et al. (2019). Key findings are detailed below.

The CFD results were compared to laser Doppler velocimetry (LDV) velocity measurements collected from the USACE Engineer Research and Development Center (ERDC) 1:25 scale physical model for multiple operating points. Figure 31 shows velocity comparisons with the points colored by sampling location. The narrow range of values in the absence of the extended-length submersible bar screen (ESBS; a screen in the intake that redirects fish into bypass structures) shows that the flow conditions develop more uniformly within the intake at the Above 1% operating point without screens than with screens for the same operating point. The above 1% operating condition corresponds to the highest flow rate to achieve a turbine efficiency within 1% of the peak efficiency for a given head. Because most of the data points lie near the 1:1 line, Serkowski et al. considered the agreement between physical and numerical models to be satisfactory.
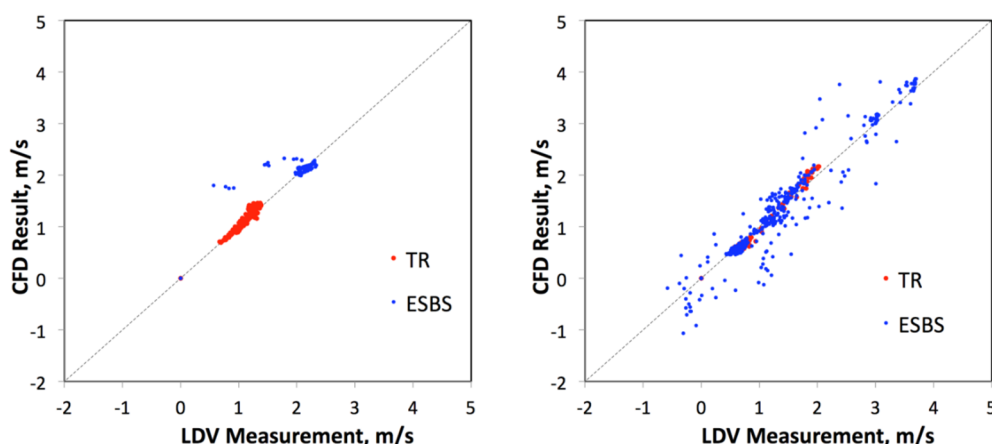

Figure 31. One-to-one velocity comparisons (stream-wise direction) from CFD (PNNL) and LDV (ERDC) at Above 1% operating point w/o screen (left) and w/ (right).

Figure 32 and Figure 33 show the vertical mean velocity profiles for CFD and ERDC models downstream of the ESBS location in Bay A. The comparison of physical and CFD model data shows a better agreement for the stream-wise component than for the vertical component. The vertical component shows a stronger cross-intake variability for the LDV measurement than for the CFD results. For the case with the ESBS deployed, there is an underestimation of the ESBS blockage effect.
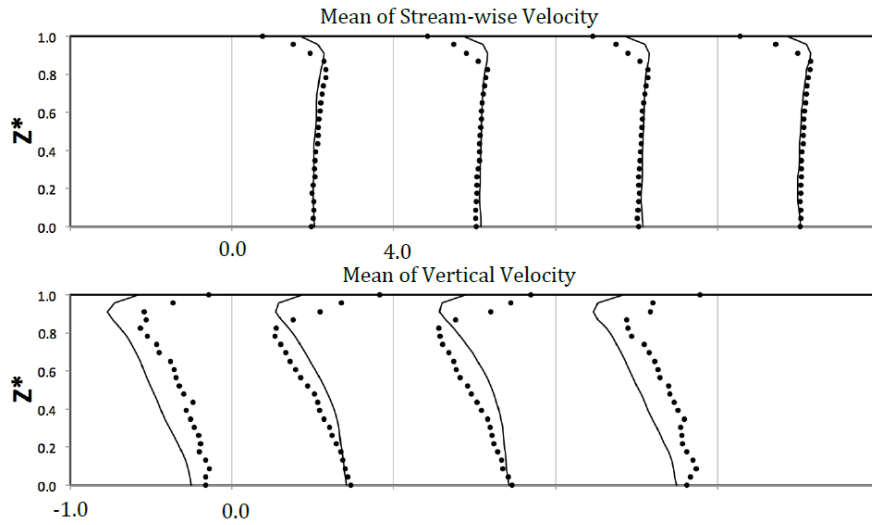
Figure 32. Vertical distribution of stream-wise and vertical velocities (in m/s) at LDV measurement locations downstream of ESBS location, at Above 1% w/o ESBS (ERDC = filled circles; CFD = line; Serkowski et al. 2019)
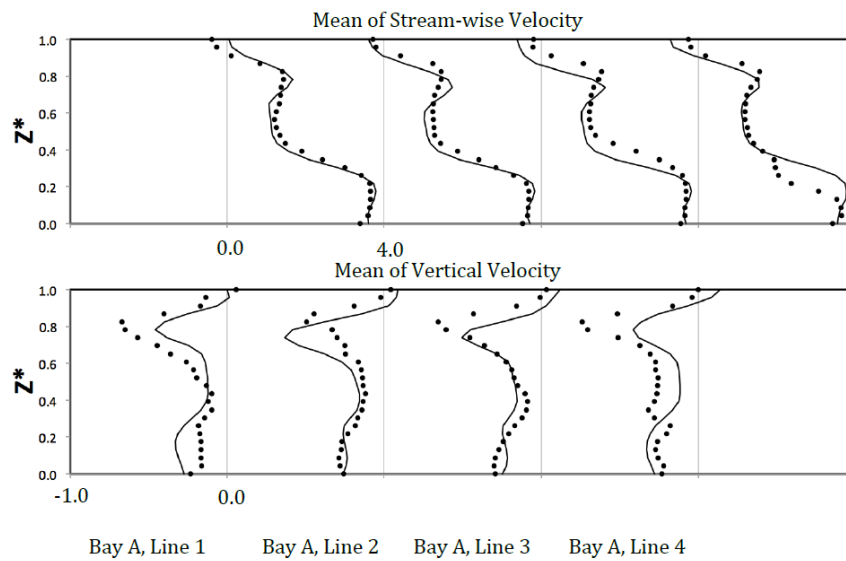

Figure 33. Vertical distribution of stream-wise and vertical velocities (in m/s) at LDV measurement locations downstream of ESBS, at Above 1% with ESBS (ERDC = filled circles; CFD = line; Serkowski et al. 2019)

Figure 34 shows a vector plot in Bay A for the Above 1% operating point with ESBS. The data, and other data detailed by Serkowski et al. (2019), provided confidence in the ability of the CFD model to match data from the reduced-scale physical models and an inferred confidence to match prototype conditions for Kaplan turbines on the Columbia River and Lower Snake River systems.
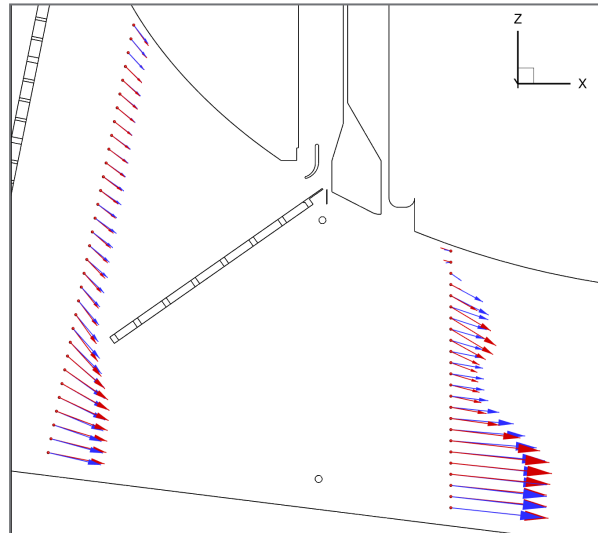

Figure 34. Vector plots of Line 2, Bay A for the operating point AB1-wE. CFD results are in red, LDV data are in blue.

5. Conclusion

As demonstrated in this report, Version 3.0 of the BioPA toolset successfully combines CFD particle trajectories with laboratory-developed biological response models to predict the probabilities of exposure to stressors for fish passing through hydropower units and facilities. Eliminated in this version of the toolset is the need for post-processing software, which in previous versions was used to compute streamlines for the trajectory/path of fish. The new version was validated through comparisons to observed physical experiments and established analytical theory. Predicted collisions and deflections closely matched the theoretical expectations in terms of position, velocity, and rebound trajectory. Validation included successfully calculating trajectories and collisions of small spherical and cylindrical particles in a water flume with vane arrays. Laboratory-scale Francis and Kaplan turbines were modeled, and hydraulic performance and flow fields were validated.

BioPA Version 3.0 combined with CFD analysis is suitable for simulating the passage of particles through hydroelectric facilities and turbines. When compared to physical models and experiments, Version 3.0 of the BioPA toolset offers a cost-effective means of comparing competing designs, enhancing passage routes and geometries, and improving existing turbines and facilities. Through comparison and minimization of fish stressors, a more sustainable hydro fleet may be realized.

References

Casartelli E, L Mangani, O Ryan, and A Del Rio. 2017. "Performance Prediction of the High Head Francis-99 Turbine for Steady Operation Points." *Journal of Physics: Conference Series* 782. http://dx.doi.org/10.1088/1742-6596/782/1/012007

Coutant CC, and RR Whitney. "Fish Behavior in Relation to Passage through Hydropower Turbines: A Review." *Transactions of the American Fisheries Society* 129(2):351-380. https://doi.org/10.1577/1548-8659(2000)129<0351:FBIRTP>2.0.CO;2

Harding S, M Richmond, and R Mueller. 2019. "Experimental Observation of Inertial Particles through Idealized Hydroturbine Distributor Geometry." *Water* 11(3). https://doi.org/10.3390/w11030471

Hogan TW, GF Cada, and SV Amaral. 2014. The Status of Environmentally Enhanced Hydropower Turbines. *Fisheries* 39(4):164-172. https://doi.org/10.1080/03632415.2014.897195

NTNU (Norwegian University of Science and Technology. 2019. Francis-99, Norwegian University of Science and Technology website: https://www.ntnu.edu/nvks/francis-99

Richmond M, J Serkowski, L Ebner, M Sick, R Brown, and T Carlson. 2014a. "Quantifying Barotrauma Risk to Juvenile Fish during Hydro-turbine Passage." *Fisheries Research* 154:152-164. https://doi.org/10.1016/j.fishres.2014.01.007

Richmond MC, JA Serkowski, C Rakowski, B Strickler, M Weisbeck, and C Dotson. 2014b. Computational Tools to Assess Turbine Biological Performance. *Hydro Review* 33(6).

Romero-Gomez P, R Singh, M Richmond, and S Weissenberger. 2021. "Numerical Investigation of Inertial Sphere Impaction on a Cylinder in Subcritical Flow." *Particulate Science and Technology*, In press.

Serkowski J, M Richmond, and C Rakowski. 2019. *Nadir Pressure Exposure Estimates for the Existing Turbines at McNary Dam*. PNNL–29200, Pacific Northwest National Laboratory, Richland, Washington

Siemens PLM, 2017. STAR-CCM+ v12.06.010 Documentation.

Trivedi C, MJ Cervantes, BK Gandhi, and OG Dahlhaug. 2013. "Experimental and Numerical Studies for a High Head Francis Turbine at Several Operating Points." *Journal of Fluids Engineering* 135(11). https://doi.org/10.1115/1.4024805

User Guide: Biological Performance Assessment (BioPA) Toolset. 2020, PNNL-29565. Richland, WA: Pacific Northwest National Laboratory.

Appendix A – Computation of Shear for BioPA Toolset

A.1 Theory

The expression for shear is derived from the constitutive equation. Here, a brief description is presented. Users can find its detailed derivation in any textbook on fluid mechanics.

The stress tensor can be written in the following form:

$$\sigma_{ij} = -p\delta_{ij} + \tau_{ij}$$

(A.1)

The first term on the right side of Equation (A.1) is the pressure exerted by the fluid, defined as thermodynamic pressure. The second term of the equation is the shear stress tensor that depends on the motion of the fluid.

There are nine elements in the shear stress tensor τ_{ij}. Each element of the shear stress tensor can be expressed as the linear combination of nine elements of the deformation rate tensor (ϵ_{ij}). Therefore,

$$\tau_{ij} = \frac{1}{2}\beta_{ijkl}\left(\frac{\partial u_k}{\partial x_i} + \frac{\partial u_i}{\partial x_k}\right)$$

(A.2)

For the isotropic condition of fourth rank tensor,

$$\beta_{ijkl} = \lambda\delta_{ij}\delta_{kl} + \mu\left(\delta_{ik}\delta_{jl} + \delta_{il}\delta_{jk}\right) + \gamma\left(\delta_{ik}\delta_{jl} - \delta_{il}\delta_{jk}\right)$$

(A.3)

here, λ, μ and γ are scalar coefficients. Note that the stress is a symmetric tensor; therefore, the coefficient γ should be zero.

$$\tau_{ij} = \frac{1}{2}\left[\lambda\delta_{ij}\delta_{kl} + \mu\left(\delta_{ik}\delta_{jl} + \delta_{il}\delta_{jk}\right)\right]\left(\frac{\partial u_k}{\partial x_i} + \frac{\partial u_i}{\partial x_k}\right)$$

(A.4)

For $l = k$ and interchanging the indices of tensor leads to

$$\tau_{ij} = \lambda\delta_{ij}\frac{\partial u_k}{\partial x_k} + \mu\left(\frac{\partial u_i}{\partial x_j} + \frac{\partial u_j}{\partial x_i}\right)$$

(A.5)

Here, nine elements of the shear stress tensor are expressed in the terms of velocity gradients. The term μ is the coefficient of dynamic viscosity. The term λ is referred to as second viscosity coefficient. For an incompressible flow, the term $\partial u_k/\partial x_k = 0$. Therefore, the shear stress term for an incompressible fluid can be expressed as

$$\tau_{ij} = \mu\left(\frac{\partial u_i}{\partial x_j} + \frac{\partial u_j}{\partial x_i}\right) = \mu S_{ij}$$

(A.6)

The magnitude of a shear tensor can be computed using the formula for Euclidian/Frobenius norm symmetric tensor. It can be computed as

$$\|S\| = \sqrt{2 S_{ij} S_{ij}}$$

(A.7)

Special Case: For the simple shear flow,

$$u = u(y)$$

$$v = w = 0$$

Therefore, only two terms exist in the shear stress tensor:

$$\tau_{xy} = \tau_{yx} = \mu\frac{du}{dy}$$

A.2 Implementation in Star-CCM+

The stress tensor in a symmetric tensor and can be implemented via a field function of the magnitude of the symmetric tensor. The symmetric tensor can be expressed via either upper triangulation or lower triangulation.

$$S = \begin{bmatrix} S_{xx} & S_{xy} & S_{xz} \\ S_{yx} & S_{yy} & S_{yz} \\ S_{zx} & S_{zy} & S_{zz} \end{bmatrix}$$

Here, $S_{xy} = S_{yx}$, $S_{xz} = S_{zx}$ and $S_{yz} = S_{zy}$ because they are symmetric. The components of the shear tensor are computed as

$$S_{xx} = 2\frac{\partial u}{\partial x}$$

$$S_{yy} = 2\frac{\partial v}{\partial y}$$

$$\varepsilon_{zz} = 2\frac{\partial w}{\partial z}$$

$$S_{xy} = S_{yx} = \left(\frac{\partial u}{\partial y} + \frac{\partial v}{\partial x}\right)$$

$$S_{xz} = S_{zx} = \left(\frac{\partial u}{\partial z} + \frac{\partial w}{\partial x}\right)$$

$$S_{yz} = S_{zy} = \left(\frac{\partial w}{\partial y} + \frac{\partial v}{\partial z}\right)$$

In Star-CCM+, S can be expressed as

Lower triangulation: $[S_{xx}; S_{yx}, S_{yy}; S_{zx}, S_{xy}, S_{zz}]$

Upper triangulation: $[S_{xx}, S_{xy}, S_{xz}; S_{yy}, S_{yz}; S_{zz}]$

To define the viscous part of the tensor, the temporary storage should be turned on as follows:

Solver $\Rightarrow$ Segregated Flow $\Rightarrow$ Check in Temporary Storage Retained.
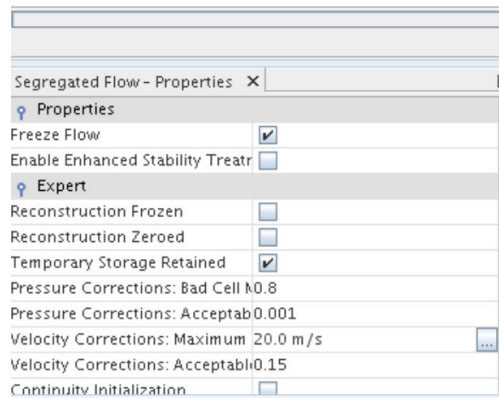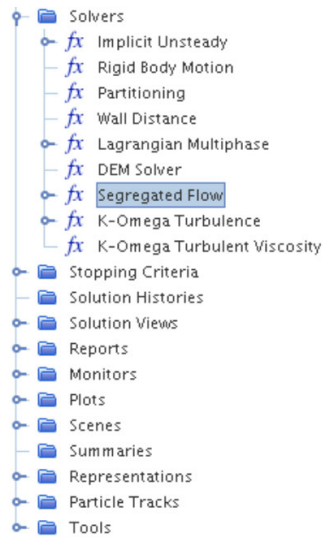
The component of the velocity gradient can be defined via the vector field function.
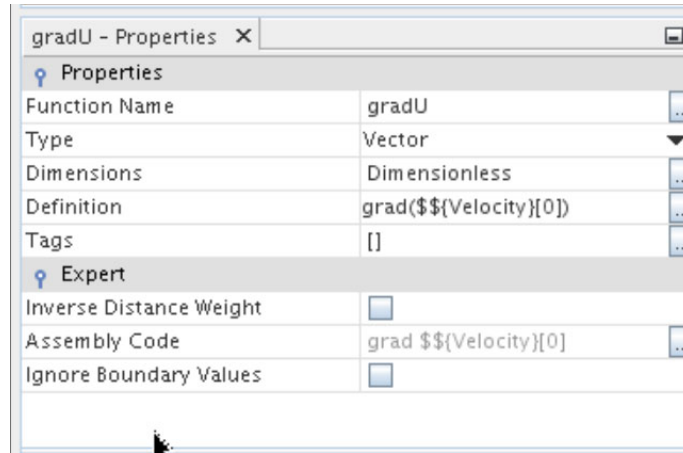
The gradient of the u velocity can be defined as
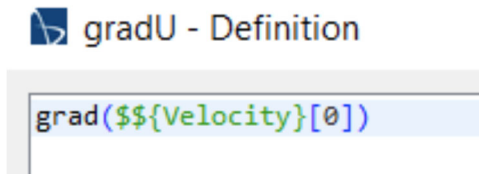
Similarly, gradient of the v and w velocity needs to be defined.

The next step is to define the stress tensor as symmetric tensor as:
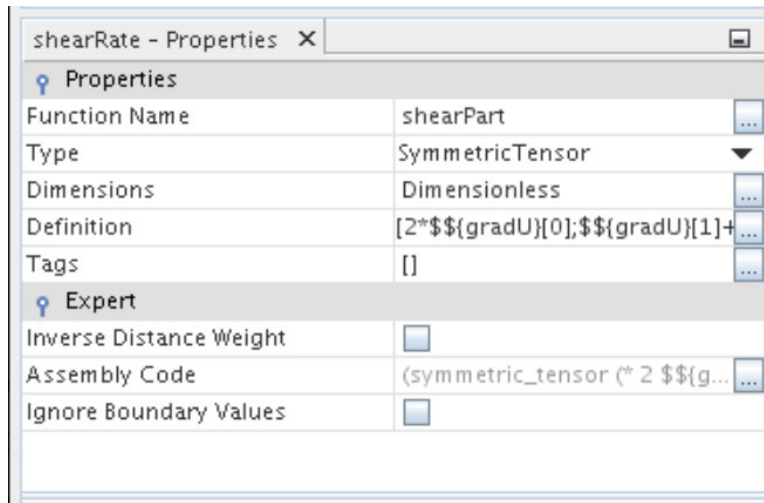
shearPart:

```
[2*$${gradU}[0];$${gradU}[1]+$${gradV}[0],2*$${gradV}[1];$${gradU}[2]+$${gradW}[0],$${gradV}[2]+$${gradW}[1],2*$${gradW}[2]]
```

[2*$${gradU}[0];$${gradU}[1]+$${gradV}[0],2*$${gradV}[1];$${gradU}[2]+$${gradW}[0],$${gradV}[2]+$${gradW}[1],2*$${gradW}[2]]

Finally, the magnitude of shear can be defined as another field function:

shearMag:

```
sqrt(2*dot($$${shearPart},$$${shearPart}))
```

Pacific Northwest
National Laboratory

902 Battelle Boulevard
P.O. Box 999
Richland, WA 99354
1-888-375-PNNL (7665)

www.pnnl.gov